PHYSICAL REVIEW B **86**, 064519 (2012)

Global superfluid phase diagram of a three-component fermion mixture with magnetic ordering

M. Kanász-Nagy and G. Zaránd

Freie Universität Berlin, Fachbereich Physik, Arnimallee 14, D-14195 Berlin, Germany and
BME-MTA Exotic Quantum Phases "Lendület" Group, Institute of Physics, Budapest University of Technology and Economics,
Budafoki út 8, H-1521 Hungary

(Received 11 April 2012; revised manuscript received 24 July 2012; published 20 August 2012)

We investigate a three-component fermion mixture in the presence of weak attractive interactions. We use a combination of the equation of motion and the Gaussian variational mean-field approaches, which both allow for simultaneous superfluid and magnetic ordering in an unbiased way, and capture the interplay between the two order parameters. This interplay significantly modifies the phase diagram, especially the superfluid-normal phase boundaries. In the close vicinity of the critical temperature and for small chemical potential imbalances, strong particle-hole symmetry breaking leads to a phase diagram similar to the one predicted by Cherng *et al.* [Phys. Rev. Lett. **99**, 130406 (2007)], however, the overall phase diagram is markedly different: additional chemical potential-driven first- and second-order transitions and triple points emerge as well as more exotic second-order multicritical points, and bicritical lines with O(2,2) symmetry. We identify the terms which are necessary to capture this complex phase diagram in a Ginzburg-Landau approach, and determine the corresponding coefficients.

DOI: 10.1103/PhysRevB.86.064519 PACS number(s): 67.60.−g, 37.10.De, 74.25.Dw

I. INTRODUCTION

Experiments with ultracold atoms opened a fascinating way to study strong correlations and the emergence of exotic phases in a controlled way.[1] Paradigmatic solid state physics models such as the fermionic and bosonic Hubbard models have been realized, and Mott insulating and magnetic phases[2,3] as well as various kinds of fermionic[4–9] and bosonic[2,10] superfluid phases have been observed. Topological excitations, e.g., vortices,[7,9] solitons,[11] two- and three-dimensional (2D and 3D) skyrmionic excitations,[12] and knot configurations[13] have been subjects of intensive research. Introduction of artificial gauge fields has also been considered both theoretically and experimentally,[14] indicating that the realization of the quantum-Hall effect and related phenomena with cold atoms are within reach.

Cold-atomic systems provide, however, not only a way to study models emerging in solid state physics, but they were also proposed to be used to mimic phenomena appearing in high-energy and particle physics. In particular, attractive three-component mixtures have been proposed to simulate quark color superfluidity[15] and "baryon" formation,[16] two fundamental concepts of quantum chromodynamics (QCD). An experimental realization of these mixtures is very difficult, but not hopeless: although three-component systems are plagued by three-particle losses,[17–19] nevertheless, Fermi degeneracy has been reached in ^{6}Li systems,[20] which may be just stable enough to reach interesting phases such as the trionic ("baryonic") regime.[17] Also, systems with closed s shells, similar to Yb, may provide an alternative and more stable way to realize almost perfectly SU(N) symmetrical states.[21,22]

In this paper, we focus on the weak-coupling regime of an attractive three-component mixture, and study its low-temperature color superfluid phases. Our main purpose is to study the effect of chemical potential differences, and provide a complete phase diagram for the SU(3) symmetrical interaction, which can be considered as the three-component analog of the famous phase diagram of Sarma.[23] Surprisingly, although several studies have been reported so far, such a phase diagram has not been discussed in sufficient detail so far, not even in the weak-coupling regime considered here. The first analysis of Ref. 15 assumed complete SU(N) symmetry and has not considered the effect of different chemical potentials. It neglected furthermore the coupling between ferromagnetic and superconducting order parameters. However, as later noticed in Refs. 16 and 24, SU(3) symmetry allows for a coupling between magnetic and superfluid order parameters, and the onset of superfluidity is therefore naturally accompanied by a ferromagnetic polarization[24,25] and possibly domain formation.[16] The consequences of such coupling have been explored in Ref. 24 in the immediate vicinity of the SU(3) symmetric phase transition using a Ginzburg-Landau approach, however, the regime of lower temperatures has not been investigated.

Throughout this paper, we shall proceed in the spirit of local density approximation (LDA) and focus on a homogeneous system of three interacting fermion species, described by the Hamiltonian

$$H = \sum_{\alpha} \int d^3\mathbf{r}\, \Psi^\dagger_\alpha(\mathbf{r})\, (\mathcal{H}_0 - \mu_\alpha)\, \Psi_\alpha(\mathbf{r}) - \sum_{\alpha\neq\beta} \lambda_{\alpha\beta} \int d^3\mathbf{r}\, \Psi^\dagger_\alpha(\mathbf{r})\Psi^\dagger_\beta(\mathbf{r})\Psi_\beta(\mathbf{r})\Psi_\alpha(\mathbf{r}). \tag{1}$$

Here, $\Psi^\dagger_\alpha(\mathbf{r})$ creates a fermion in a hyperfine state $\alpha = 1,2,3$ with corresponding chemical potentials μ_α. The interaction between the species is assumed to be local and attractive ($\lambda_{\alpha\beta} > 0$ for $\alpha \neq \beta$).[26] Furthermore, throughout most of this work, we shall also assume SU(3) symmetrical interactions $\lambda_{\alpha\beta} = \lambda$ for $\alpha \neq \beta$. This assumption is certainly justified for Yb-like closed s-shell systems, and is also a valid approximation for the ^{6}Li system in the high magnetic field limit.[27] Although the scattering lengths in the lowest three hyperfine states are slightly different in the latter system, one can use radio frequency and microwave fields to make them equal up to ~0.1% accuracy.[28]

The particular form of the single-particle operator $\mathcal{H}_0$ in Eq. (1) is not very important since $\mathcal{H}_0$ enters the mean-field calculations only through the corresponding single-particle density of states (DOS), for which we assume a simple form $\rho(\xi) = \rho_0(1 + \gamma\ \xi)$ and a rigid bandwidth cutoff at $\xi = \pm W$. Keeping the linear term $\rho_0\gamma\ \xi$ is crucial: this term, characterizing in some sense the particle-hole symmetry breaking (see Sec. II C), is the primary source of the coupling between ferromagnetic and superfluid order parameters. Note that in the small-coupling regime, only the DOS ρ_F at the Fermi energy and its first derivative are expected to have considerable impact in the phase diagram, and therefore we do not need to go beyond this simple linear approximation. We should remark though that the interactions renormalize the chemical potentials, and therefore the position of the renormalized Fermi energy ξ_F and the corresponding single-particle density of states ρ_F must be determined self-consistently.[29]

Although we also discuss to a certain extent the role of fluctuations in Sec. V, the bulk of this work consists of a mean-field analysis. Even this is, however, not entirely trivial. In the Hubbard-Stratonovich approach of Refs. 30 and 24, the decoupling of the interaction into ferromagnetic and superfluid parts suffers from a certain degree of arbitrariness.[31] Treating the ferromagnetic and superfluid order parameters at equal footing therefore requires care. Furthermore, at lower temperatures the second-order transitions turn into first-order transitions, and the free energy develops several inequivalent local minima, as has been pointed out in the case of two-component mixtures by Sarma.[23] To cope with these difficulties, we applied two complementary methods: an equation of motion method (EOM) with systematically neglected vertex corrections, which leads to mean-field self-consistency equations, and a Gaussian variational approach, which consists of finding the minima of a mean-field free energy. Both approaches are exempt from the arbitrariness of the Hubbard-Stratonovich transformation, account for the interplay between ferromagnetic and superfluid order, and, remarkably, they are entirely *consistent* since at the saddle points of the variational mean-field free energy, the EOM self-consistency equations are satisfied (see Sec. II B). However, the Gaussian variational approach is more efficient in that it provides an estimate for the mean-field free energy also away from the free-energy saddle points, and therefore it allows us to locate first-order transitions in a complicated free-energy landscape. Since previous works on two-component mixtures indicate that the Fulde-Ferrell-Larkin-Ovchinnikov (FFLO) phase with spatially varying order parameter[32,33] appears only in a tiny region of the phase diagram,[6,7] here we restrict our investigation to spatially homogeneous phases. We shall neither consider breached pair (BP) nor Sarma phases[23,34] since these would require fermions of very different masses.

Before we turn to the more detailed presentation of the calculations, let us summarize here our most important results. In the small-coupling limit, where the critical temperature at the SU(3) symmetric point satisfies $T_c \approx 1.13\,W\,e^{-1/(2\lambda\rho_F)} \ll W$,[35,36] the phase diagram is expected to become universal for SU(3) symmetrical interactions: it should depend only on the dimensionless temperature T/T_c, the dimensionless chemical potential shifts $\delta\mu_\alpha/T_c$, and the dimensionless particle-hole symmetry-breaking parameter $\tilde{\gamma} \equiv \gamma T_c$,[37] defined in terms of the critical temperature T_c at the SU(3) symmetrical point $\mu_\alpha \equiv \mu$. Figure 1 shows the corresponding schematic phase diagram in case of a particle-hole symmetrical situation $\gamma = 0$.[37] The bottom figure shows a finite-temperature cut of the phase diagram as a function of the chemical potential differences[38]

$$\mu_x \equiv (\mu_1 - \mu_2)/\sqrt{2}\,, \quad \mu_y \equiv (\mu_1 + \mu_2 - 2\mu_3)/\sqrt{6}$$

for a temperature T fixed somewhat below the SU(3) symmetrical transition temperature T_c and a fixed average chemical potential $\bar{\mu} \equiv (\mu_1 + \mu_2 + \mu_3)/3$. In the various gray regions, two species of the smallest chemical potential difference pair up to form a superfluid (SF) state, while the third species remains gapless.[39] This explains the starlike structure of the phase diagram: superfluid phases appear around regions, where two of the chemical potentials become equal. As we discuss in Sec. II C, the high ("hexagonal") symmetry of the figure is a direct fingerprint of the SU(3) symmetrical interaction, and a discrete particle-hole symmetry. The superfluid state is destroyed once all chemical potential differences become large compared to the condensation energy (white region). Close to T_c, the chemical-potential-driven SF-normal transitions are of second order (black lines), just as in case of

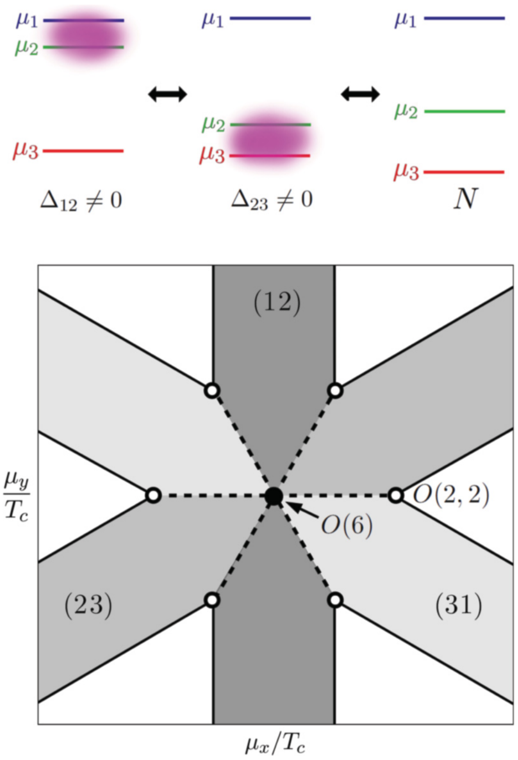

FIG. 1. (Color online) Sketch of the phase diagram for a constant DOS, and chemical potential shifts $\delta\mu_1 + \delta\mu_2 + \delta\mu_3 = 0$. Top: SF forms between fermions with the closest chemical potentials, whereas at higher differences the normal state (N) is favored. Bottom: Cut of the SF phase diagram for $T \lesssim T_c$. Apart from the special points (full and empty circles) SF order always forms in one of the channels (12), (23), or (31). At the point $\mu_x = \mu_y = 0$ (full circle), the Hamiltonian is SU(3) symmetric, and the transition is described by an O(6) critical point. The first-order lines, separating different SF phases, terminate in second-order critical points with O(2,2) symmetry (empty circles). Different SF orders are denoted by different grayscale colors.

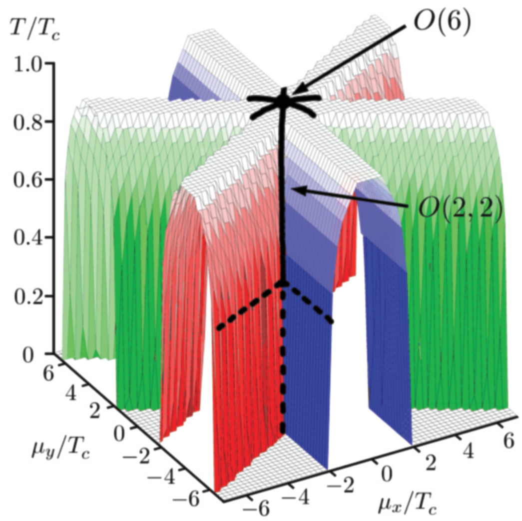

FIG. 2. (Color online) Numerically computed SF-N phase boundary as a function of the chemical potentials at constant DOS for $\lambda\rho_F = 0.1$, and $\gamma = \xi_F = 0$, corresponding to $T_c/W = 0.0076$. The SF-N transition becomes of first order below a temperature $\widetilde{T}^{\,\mathrm{Sarma}}$ (horizontal dashed lines). Vertical lines denote the O(2,2) critical points of second (solid line) and of first order (dashed line).

a two-component mixture.[23] The transition between *different* SF phases is, however, always of first order (dashed lines).

The phase diagram also exhibits some interesting points of special symmetry. At the point $\mu_x = \mu_y = 0$, the Hamiltonian is SU(3) symmetrical, and correspondingly, the phase transition at $T = T_c$ and $\mu_x = \mu_y = 0$ is described by an O(6) theory (the six components corresponding to the real and imaginary parts of the superfluid order parameters). In three dimensions, this symmetry is spontaneously broken for $T < T_c$.[30,40] On the other hand, at the points indicated by white circles in Fig. 1, the competition of two order parameters most likely leads to a so-called O(2,2) critical behavior (see Sec. V).

Figure 2 shows the numerically obtained phase diagram in a three-dimensional plot under the assumption of SU(3) symmetric interaction and particle-hole symmetry ($\gamma = 0$).[37] The domelike structures correspond to superfluid phases with pairing in the (12), (23), and (31) channels. Below the horizontal dashed lines, the chemical potential driven phase transitions become of first order, while above these lines they are of second order, as we point out in Secs. III A and III C. These lines are thus the analogs of the critical point identified by Sarma.[23] The SF-normal transitions on the "roofs" of the domes belong to the O(2) universality class, while the black solid lines correspond to O(2,2) critical points. Finally, the crossing of the black lines at $\mu_x = \mu_y = 0$ corresponds to an O(6) critical point.

This rich phase diagram is further complicated if one allows for particle-hole symmetry breaking $\gamma \neq 0$ (Ref. 41) (see Sec. III B). On a larger scale, the $\gamma \neq 0$ phase diagram looks quite similar to the $\gamma = 0$ phase diagrams, presented in Figs. 1 and 2, however, the structure of the phase diagram changes in the close vicinity of the SU(3) symmetrical point. This is demonstrated in Fig. 3, where the central region of the phase diagram is shown for $T = T_c$ and 0.5 T_c. The absence of particle-hole symmetry destroys the hexagonal symmetry of the phase diagram, and leads to a trigonal structure, as predicted by Cherng *et al.*[24] In this central region, a higher DOS, and thus gain in condensation energy, may make SF ordering favorable in a channel not of the smallest chemical potential difference. This effect is most spectacular at $T = T_c$, where by shifting the Fermi energy of two species one can increase the critical temperature, and induce superfluidity (see Fig. 3, top). We remark, however, that in spite of the relatively large particle-hole asymmetry introduced, this central region is typically quite small compared to the rest of the phase diagram, at least for weak couplings $T_c \ll W$. The orientation of the phases is, however, opposite to the one predicted in Ref. 24: to obtain the same orientation, we need to flip the sign of the slope of the DOS, and assume a holelike Fermi surface $\gamma < 0$. We remark that the orientation we find can be understood on simple physical arguments (see Sec. III B). We must also add here that the Ginzburg-Landau action of Ref. 24 is unable to capture the endpoints of the "trigonal" region, and one must

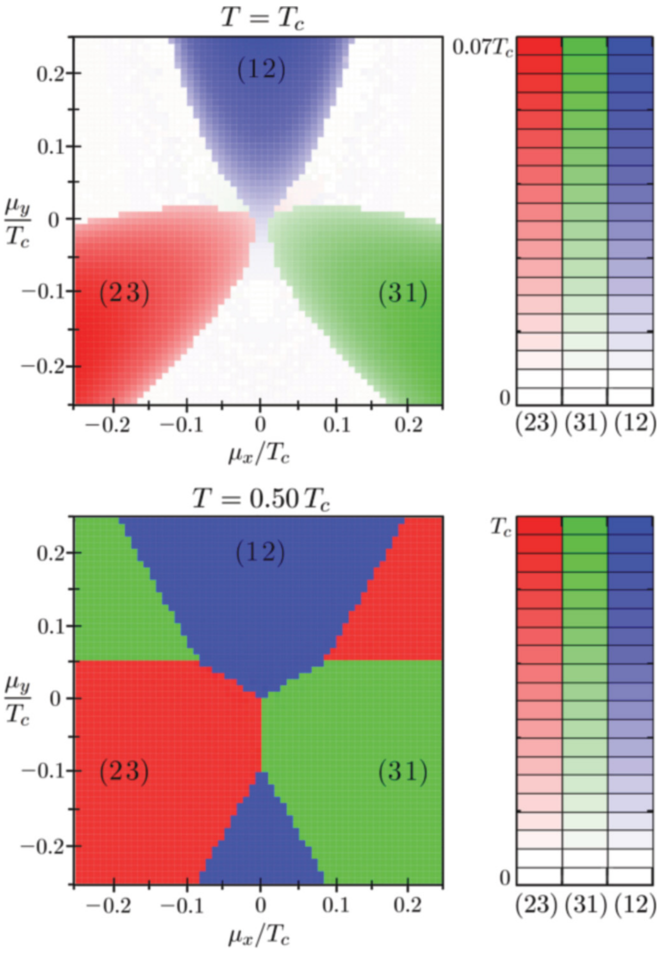

FIG. 3. (Color online) Phase diagram in the vicinity of the SU(3) symmetric point in the absence of particle-hole symmetry $\gamma \neq 0$. The sixfold symmetry of the phase diagram is destroyed. A higher DOS can make SF ordering favorable in a channel not of the smallest chemical potential difference, due to the gain in condensation energy. For the absolute values of the SF order parameters Δ_{ij}, see the respective color (gray) scales (right). Parameters at the SU(3) symmetric point: $\lambda\,\rho_F = 0.112$, $\gamma W = 0.5$, $T_c/W = 0.011$, $\xi_F/W = 0.24$ (half-filling).

retain higher-order terms in the action to account for these (see Sec. IV).

The rest of the paper is organized as follows: In Sec. II, we introduce our mean-field methods. We also discuss the symmetries of the order parameters, leading to rather strong constraints on the form of the phase diagram. In Sec. III, we present our main results on the SF phase diagram, with and without particle-hole symmetry, and compare our findings with results on two component systems. In Sec. IV, we present the numerical Ginzburg-Landau expansion of the free energy around the SU(3) symmetric point, and identify the terms responsible for the main features of the central part of the phase diagram. In Sec. V, we discuss the effect of fluctuations in the special O(2,2) symmetric bicritical points. In Sec. VI, we comment on the experimental realizability of an SU(3) symmetric system. Some of the technical details of our calculations can be found in the Appendixes.

II. MEAN-FIELD CALCULATIONS

In this section, we first use an imaginary-time equation of motion method to derive the self-consistency equations for the SF and magnetic order parameters. Then, to address the low-temperature regime, where these equations have multiple solutions,[23] we also develop a Gaussian variational approximation. This approach provides an estimate for the free energy and enables one to locate first-order transitions.

A. Equation of motion technique

To simplify our notation, let us first introduce the six-component Nambu spinor field

$$\Phi(x) = (\Psi(x), \Psi^\dagger(x))^T \; .$$

Here, we used the compact notation $x = (\mathbf{r},\tau)$ for the space and imaginary-time coordinates. The corresponding 6×6 propagator matrix $\mathbf{D}(x_1,x_2) \equiv -\langle T_\tau\, \Phi(x_1) \circ \Phi^\dagger(x_2)\rangle$ contains the normal as well as the anomalous Green's functions of the fields $\Psi_\alpha(x)$ and, assuming spatial homogeneity, also obeys $\mathbf{D}(x_1,x_2) = \mathbf{D}(x_1 - x_2)$. In order to derive equation of motion for the propagators, we start from the imaginary-time equation of motion (EOM) of the fields,

$$\partial_\tau \Psi_\alpha(x) = [H, \Psi_\alpha(x)]\, . \tag{2}$$

The EOM of the part $-\langle \mathrm{T}_\tau \Psi_\alpha(x_1)\Psi^\dagger_\beta(x_2)\rangle$ of the propagator follows from Eq. (2), and reads as

$$\begin{aligned}(\partial_{\tau_1} + \mathcal{H}_0(\mathbf{r}_1) - \mu_\alpha)\langle \mathrm{T}_\tau \Psi_\alpha(x_1)\Psi^\dagger_\beta(x_2)\rangle \\ = \delta_{\alpha\beta}\delta_{x_1x_2} + \sum_\gamma 2\lambda_{\alpha\gamma}\langle \mathrm{T}_\tau \Psi^\dagger_\gamma(x_1)\Psi_\gamma(x_1)\Psi_\alpha(x_1)\Psi^\dagger_\beta(x_2)\rangle,\end{aligned} \tag{3}$$

with $\delta_{x_1x_2}$ denoting the four-dimensional Dirac-delta function. Similar equations hold for the anomalous propagators $-\langle \mathrm{T}_\tau \Psi_\alpha(x_1)\Psi_\beta(x_2)\rangle$ and $-\langle \mathrm{T}_\tau \Psi^\dagger_\alpha(x_1)\Psi^\dagger_\beta(x_2)\rangle$.

To make further progress, we simplify the four-point functions appearing in these EOMs by simply neglecting the vertex contribution, as shown in Fig. 4. This approximation is almost equivalent to the usual BCS approximation, however, it goes beyond that since it allows for the simultaneous appearance of different kinds of order parameters in an unbiased way. Furthermore, even in the simple SU(2) case, it also incorporates, e.g., the renormalization of the Pauli susceptibility at the mean- field level (see Sec. III C). With this approximation, the equation of motion becomes solvable, and the Nambu propagator is found to take the following form in Fourier space:

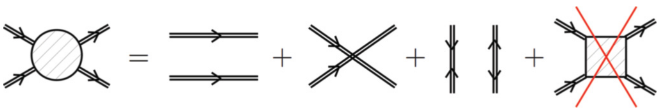

FIG. 4. (Color online) Omission of the vertex corrections in the connected four-point functions (left-hand side). Heavy lines denote the full propagators, and the square stands for the vertex contribution.

$$\mathbf{D}(i\omega_n,\mathbf{k})^{-1} = i\omega_n - \mathbf{B}(\xi_{\mathbf{k}}). \tag{4}$$

Here, $\omega_n = (2n+1)\pi T$ are fermionic Matsubara frequencies and the matrix $\mathbf{B}(\xi)$ is defined as

$$\mathbf{B}(\xi) \equiv \begin{pmatrix} \xi - \mathbf{\Lambda} & 2\mathbf{\Delta} \\ 2\mathbf{\Delta}^+ & -(\xi - \mathbf{\Lambda}^*) \end{pmatrix}. \tag{5}$$

The matrices

$$\Delta_{\alpha\beta} \equiv \lambda_{\alpha\beta} d_{\alpha\beta}, \tag{6}$$

$$\Lambda_{\alpha\beta} \equiv \left(\mu_\alpha + 2\sum_\gamma \lambda_{\alpha\gamma} n_{\gamma\gamma}\right)\delta_{\alpha\beta} - 2\lambda_{\alpha\beta} n^*_{\alpha\beta} \tag{7}$$

denote the SF order parameter[42] and the renormalized chemical potential, respectively. They are defined in terms of the matrix of densities $\mathbf{n}$, and that of the anomalous densities $\mathbf{d}$:

$$n_{\alpha\beta} \equiv \langle \Psi^\dagger_\alpha(x_1)\Psi_\beta(x_1)\rangle, \tag{8}$$

$$d_{\alpha\beta} \equiv \langle \Psi_\alpha(x_1)\Psi_\beta(x_1)\rangle. \tag{9}$$

The matrices $\mathbf{n}$ and $\mathbf{d}$ can be used to describe magnetic and SF ordering, respectively. However, it is more natural to use $\mathbf{\Lambda}$ and $\mathbf{\Delta}$ as order parameters. Note that, according to Eq. (7), magnetic ordering implies a shift in the renormalized chemical potential $\Lambda_{\alpha\beta}$, and this shift can thus also be considered as a magnetic order parameter.

The expectation values Eqs. (8) and (9) are given by the propagator $\mathbf{D}(x_1 - x_2)$ at equal times and equal positions, and are thus determined by Eq. (4). By taking the inverse of Eq. (4) and performing the Matsubara summation over the frequencies ω_n, we obtain

$$\int_{-W}^{W} d\xi\, \rho(\xi)\, f(\mathbf{B}(\xi)) = \begin{pmatrix} \mathbf{n}^* & -\mathbf{d} \\ -\mathbf{d}^+ & -\mathbf{n} + \int d\xi\, \rho(\xi) \end{pmatrix}, \tag{10}$$

where $\rho(\xi)$ denotes the DOS of $\mathcal{H}_0$, and f stands for the Fermi function. Equations (5)–(7) and (10) thus determine self-consistently the order parameters $\mathbf{\Lambda}$ and $\mathbf{\Delta}$. We solve these equations iteratively, starting from random initial conditions, and performing the integrals in Eq. (10) numerically. Notice that $f(\mathbf{B}(\xi))$ is a matrix function, therefore, its evaluation requires numerical diagonalization of the Hermitian matrix $\mathbf{B}(\xi)$ for each value of ξ.

We remark that the matrix $\mathbf{B}(\xi)$ in Eq. (5) possesses a symplectic symmetry

$$\begin{pmatrix} \mathbf{0} & \mathbf{1} \\ \mathbf{1} & \mathbf{0} \end{pmatrix} \mathbf{B}(\xi) \begin{pmatrix} \mathbf{0} & \mathbf{1} \\ \mathbf{1} & \mathbf{0} \end{pmatrix} = -\mathbf{B}^{\mathrm{T}}(\xi) \tag{11}$$

since the order parameters $\mathbf{\Delta}$ and $\mathbf{\Lambda}$ are skew symmetric and Hermitian, respectively. This symmetry makes the eigenvalues of $\mathbf{B}(\xi)$ come in pairs $(\upsilon, -\upsilon)$, and thus simplifies some of our calculations of the free energy in the next section. It is also responsible for the structure of the equal-time, equal-position propagator in Eq. (10).

B. Gaussian variational approach

To investigate the low-temperature phase diagram, we employ a variational method. This method consists of finding the best Gaussian approximation to the free energy $F = -T \ln \mathcal{Z}$ of the system. As a first step, we express the grand-canonical partition function $\mathcal{Z}$ as a functional integral

$$\mathcal{Z} = \int \mathfrak{D}\overline{\boldsymbol{\psi}}\, \mathfrak{D}\boldsymbol{\psi}\, e^{-S[\overline{\boldsymbol{\psi}},\boldsymbol{\psi}]}, \tag{12}$$

with the action written as $S = S_0 + S_{\text{int}}$, and the noninteracting and interacting parts defined as

$$S_0 = -\frac{1}{2} \int d1\, d2\, \overline{\phi}(1)\, \mathcal{D}_0^{-1}(1,2)\, \phi(2), \tag{13}$$

$$S_{\text{int}} = -\sum_{\alpha\beta} \lambda_{\alpha\beta} \int dx\, \overline{\psi}_\alpha(x) \overline{\psi}_\beta(x) \psi_\beta(x) \psi_\alpha(x). \tag{14}$$

Here, $\phi = (\psi, \overline{\psi})^T$ is a Nambu spinor field and we used the notations "$1'' = (\mathbf{r}_1, \tau_1, \nu_1)$, and $\int d1 \ldots$ to denote the integration over space and imaginary-time variables and the summation over Nambu indices $(\nu_1 = 1, \ldots, 6)$ in a compact way. The inverse propagator

$$-\mathcal{D}_0^{-1} = \delta_{x_1 x_2} \left[\partial_{\tau_2} + \begin{pmatrix} \mathcal{H}_0 - \hat{\mu} & 0 \\ 0 & -(\mathcal{H}_0 - \hat{\mu}) \end{pmatrix} \right] \tag{15}$$

contains the single-particle Hamiltonian of the free fields $\mathcal{H}_0$, where $\hat{\mu}_{\alpha\beta} = \mu_\alpha\, \delta_{\alpha\beta}$ is a 3×3 diagonal matrix containing the chemical potentials.

Our Gaussian approximation of the free energy is based on the standard inequality[43]

$$F \leqslant F_G[\mathcal{D}] \equiv -T \ln \mathcal{Z}_{\mathcal{D}} + T \langle S - S_{\mathcal{D}} \rangle_{\mathcal{D}}\, . \tag{16}$$

Here, the partition function $\mathcal{Z}_{\mathcal{D}}$ and the average $\langle \ldots \rangle_{\mathcal{D}}$ are defined in terms of the Gaussian action

$$S_{\mathcal{D}} \equiv -\frac{1}{2} \int d1\, d2\, \overline{\phi}(1)\, \mathcal{D}^{-1}(1,2)\, \phi(2)\, , \tag{17}$$

$$\mathcal{Z}_{\mathcal{D}} \equiv \int \mathfrak{D}\overline{\boldsymbol{\psi}}\, \mathfrak{D}\boldsymbol{\psi}\, e^{-S_{\mathcal{D}}[\overline{\boldsymbol{\psi}},\boldsymbol{\psi}]}\, , \tag{18}$$

$$\langle \cdots \rangle_{\mathcal{D}} \equiv \frac{1}{\mathcal{Z}_{\mathcal{D}}} \int \mathfrak{D}\overline{\boldsymbol{\psi}}\, \mathfrak{D}\boldsymbol{\psi}\, \cdots\, e^{-S_{\mathcal{D}}[\overline{\boldsymbol{\psi}},\boldsymbol{\psi}]}\, . \tag{19}$$

Since we do not want to restrict our investigations to actions that can be associated with a Hamiltonian, we do not require $S_{\mathcal{D}}$ to be local. Nevertheless, at the saddle points of F_G, $S_{\mathcal{D}}$ turns out to be local, and there exists a Hamiltonian associated with it [see Eqs. (22)–(24) below].

Since the action $S_{\mathcal{D}}$ is quadratic, the propagator matrix of the Nambu fields can be written as

$$\mathcal{D}(1,2) = -\langle \phi(1)\, \overline{\phi}(2) \rangle_{\mathcal{D}}\, , \tag{20}$$

and expectation values can be evaluated using Wick's theorem. We remark that the choice (20) automatically fixes a certain ambiguity in the definition of $\mathcal{D}^{-1}$. (For details, see Appendix C.) The best Gaussian approximation is given by the minimum of the functional $F_G[\mathcal{D}]$, where F_G satisfies the saddle-point equation

$$\frac{\delta F_G}{\delta \mathcal{D}(1,2)} = 0. \tag{21}$$

As is shown in Appendix C, this equation is equivalent to the self-consistency equations (5), (6), (7), and (10) of the EOM technique, and amounts in $\mathcal{D}^{-1}$ being a local,

$$\mathcal{D}^{-1}(1,2) = \delta(x_1 - x_2)\, \mathbf{D}^{-1}(x_2) \tag{22}$$

with the matrix operator on the right-hand side being just the inverse propagator [Eq. (4)] in real space,

$$-\mathbf{D}^{-1} = \partial_{\tau_2} + \begin{pmatrix} \mathcal{H}_0(\mathbf{r}_2) - \mathbf{\Lambda} & 2\mathbf{\Delta} \\ 2\mathbf{\Delta}^+ & -(\mathcal{H}_0(\mathbf{r}_2) - \mathbf{\Lambda}^*) \end{pmatrix}. \tag{23}$$

The order parameters $\mathbf{\Lambda}$ and $\mathbf{\Delta}$ are determined by the former equations (6) and (7).

Thus, the Gaussian variational approach is entirely consistent with the EOM method. However, it is also more efficient since it enables us to obtain an estimate for the free energy. By Eqs. (22) and (23), to calculate the best approximation F_G to the free energy, it is sufficient to consider local actions for which we can express $S_{\mathcal{D}}$, and thus F_G, in terms of a Hamiltonian

$$H_{\mathcal{D}} = \frac{1}{2} \int d^3\mathbf{r} : \Phi^\dagger \begin{pmatrix} \mathcal{H}_0 - \mathbf{\Lambda} & 2\mathbf{\Delta} \\ 2\mathbf{\Delta}^+ & -(\mathcal{H}_0 - \mathbf{\Lambda}^*) \end{pmatrix} \Phi :. \tag{24}$$

Since the functional integrals are, by definition, normal ordered, the Hamiltonian $H_{\mathcal{D}}$ also needs to be normal ordered, as emphasized by the semicolons in Eq. (24), indicating normal ordering with respect to the vacuum.[44]

In this Hamiltonian language, Eq. (16) takes on the form

$$F_G(\mathbf{\Lambda}, \mathbf{\Delta}) = -T \ln \mathcal{Z}_{\mathcal{D}} + \langle H - H_{\mathcal{D}} \rangle_{\mathcal{D}}\, , \tag{25}$$

with H the full Hamiltonian of the system, Eq. (2), and

$$\mathcal{Z}_{\mathcal{D}} = \mathrm{Tr} e^{-\beta H_{\mathcal{D}}}, \tag{26}$$

$$\langle \cdots \rangle_{\mathcal{D}} = \mathrm{Tr}(\cdots e^{-\beta H_{\mathcal{D}}}) / \mathcal{Z}_{\mathcal{D}}\, . \tag{27}$$

Notice that $F_G(\mathbf{\Lambda}, \mathbf{\Delta})$ also depends implicitly on the chemical potentials μ_α and the temperature T, and it must be minimized to find the mean-field value of the variational parameters $\mathbf{\Lambda}(\mu_\alpha, T)$ and $\mathbf{\Delta}(\mu_\alpha, T)$.

In this Hamiltonian approach, the evaluation of Eq. (25) is straightforward (see Appendix D), and for the free-energy density we obtain

$$f_G = \frac{1}{2} \int d\xi\, \rho(\xi) \mathrm{Tr}(\xi - \mathbf{\Lambda}) - \frac{T}{2} \int d\xi\, \rho(\xi) \mathrm{Tr} \ln \{2 \cosh [\beta\, \mathbf{B}(\xi)/2]\}$$

$$+\sum_{\alpha\beta}[(\boldsymbol{\Lambda}_{\alpha\beta}-\mu_\alpha\delta_{\alpha\beta})\mathbf{n}_{\alpha\beta}+\lambda_{\alpha\beta}(|\mathbf{n}_{\alpha\beta}|^2-\mathbf{n}_{\alpha\alpha}\mathbf{n}_{\beta\beta})]$$
$$+\sum_{\alpha\beta}(\boldsymbol{\Delta}_{\alpha\beta}\mathbf{d}^*_{\alpha\beta}+\boldsymbol{\Delta}^*_{\alpha\beta}\mathbf{d}_{\alpha\beta}-\lambda_{\alpha\beta}|\mathbf{d}_{\alpha\beta}|^2). \qquad (28)$$

Here, $\beta = 1/T$ is the inverse temperature, the densities $\mathbf{n}$ and $\mathbf{d}$ are determined by Eq. (10), and the matrix $\mathbf{B}(\xi)$ is defined in Eq. (5).

As stated before, at the local minima of the functional f_G, the order parameters $\boldsymbol{\Lambda}$ and $\boldsymbol{\Delta}$ fulfill the EOM self-consistency equations. In our numerical calculations, however, we have not enforced this constraint. Rather, we treated the order parameters as independent and free variables, and used a Monte Carlo method to find the absolute minimum of Eq. (28) in the 15-dimensional space spanned by these order parameters. In the end, we verified numerically that at the minima, $\boldsymbol{\Lambda}$ and $\boldsymbol{\Delta}$ indeed satisfy the EOM self-consistency equations.

A comparison of the variational Monte Carlo approach and the straightforward solution of the EOM self-consistency equations is presented in Fig. 5. At low temperatures, the EOM becomes unreliable in the vicinity of first-order phase boundaries, and finds several possible local minima. The variational Monte Carlo method (with simulated annealing), however, finds the absolute minimum of the free energy f_G and is able to identify the physically relevant solution.

C. Symmetries

For an SU(3) symmetrical interaction $\lambda_{\alpha\beta} = \lambda$ for $\alpha \neq \beta$, the structure of the phase diagram is largely determined by the underlying SU(3) symmetry. In particular, for $\mu_\alpha \equiv \mu$ the Hamiltonian is invariant under global SU(3) rotations $\Psi_\alpha(x) \mapsto \sum_\beta U_{\alpha\beta}\Psi_\beta(x)$ and a global U(1) gauge transformation $\Psi_\alpha(x) \mapsto e^{i\varphi}\,\Psi_\alpha(x)$.

The ferromagnetic order parameters $\mathbf{n}$ and $\boldsymbol{\Lambda}$ are Hermitian. They are invariant under the U(1) gauge transformation, and transform under SU(3) rotations as

$$\mathbf{n}^{\mathrm{T}} \mapsto \mathbf{U}\,\mathbf{n}^{\mathrm{T}}\mathbf{U}^\dagger, \quad \boldsymbol{\Lambda} \mapsto \mathbf{U}\,\boldsymbol{\Lambda}\mathbf{U}^\dagger, \qquad (29)$$

which, after taking out the trivial trace, is equivalent to the eight-dimensional adjoint representation of SU(3).

The order parameters $\mathbf{d}$ and $\boldsymbol{\Delta}$ are, on the other hand, skew symmetric, transform as $\mathbf{d} \mapsto e^{i2\varphi}\,\mathbf{d}$ and $\boldsymbol{\Delta} \mapsto e^{i2\varphi}\,\boldsymbol{\Delta}$ under U(1) gauge transformations, and the global SU(3) group transforms them according to

$$\mathbf{d} \mapsto \mathbf{U}\,\mathbf{d}\mathbf{U}^{\mathrm{T}}, \quad \boldsymbol{\Delta} \mapsto \mathbf{U}\,\boldsymbol{\Delta}\mathbf{U}^{\mathrm{T}}, \qquad (30)$$

which is equivalent to the conjugate representation of SU(3). This can be seen by introducing the three-component vectors $\underline{d}_\alpha = \frac{1}{2}\sum_{\beta\gamma}\epsilon_{\alpha\beta\gamma}d_{\beta\gamma}$ and $\underline{\Delta} = \frac{1}{2}\sum_{\beta\gamma}\epsilon_{\alpha\beta\gamma}\Delta_{\beta\gamma}$ by means of the completely antisymmetric Levi-Civita symbol $\epsilon_{\alpha\beta\gamma}$. In this form, Eq. (30) reads as

$$\underline{\mathbf{d}} \mapsto \mathbf{U}^*\underline{\mathbf{d}}, \quad \underline{\boldsymbol{\Delta}} \mapsto \mathbf{U}^*\underline{\boldsymbol{\Delta}}\ . \qquad (31)$$

In the special case $\lambda_{\alpha\beta} = \lambda$ for $\alpha \neq \beta$, and $\mu_\alpha = \mu$, symmetry implies that the Ginzburg-Landau functional must be invariant under the transformations (29) and (30), and the U(1) gauge transformation. The onset of superfluidity, however, spontaneously breaks the SU(3) ⊗ U(1) symmetry down to SU(2) ⊗ U(1). This spontaneous symmetry breaking is accompanied by the emergence of five Goldstone modes.[30]

The presence of the chemical potentials $\hat{\mu}_{\alpha\beta} = \delta_{\alpha\beta}\mu_\alpha$ obviously breaks the SU(3) symmetry. However, one has strong symmetry-dictated constraints on the Ginzburg-Landau functional even in this case, and the latter must be invariant with respect to the transformations in Eqs. (29) and (30), provided that $\hat{\mu}$ is also transformed accordingly, $\hat{\boldsymbol{\mu}} \mapsto \mathbf{U}\,\hat{\boldsymbol{\mu}}\mathbf{U}^\dagger$ (see also Sec. IV). In addition, even in the presence of chemical potential differences, SU(3) symmetry implies Ward identities,[24] relating four-point expectation values and the ferromagnetic order parameter $\mathbf{n}$ as

$$(\mu_\alpha - \mu_\beta)n_{\alpha\beta} = \sum_\gamma 2(\lambda_{\beta\gamma} - \lambda_{\alpha\gamma})\langle\Psi^\dagger_\gamma\Psi^\dagger_\alpha\Psi_\beta\Psi_\gamma\rangle\ . \qquad (32)$$

From this identity (derived in Appendix A) it follows that $\mathbf{n}$ is diagonal for an SU(3) symmetric interaction. We remark that a similar approximate Ward identity can be derived within the Gaussian variational method (see Appendix B), leading to the same conclusions.

The off-diagonal elements of the chemical potential tensor $\hat{\boldsymbol{\mu}}$ describe tunneling between different hyperfine components, and they typically vanish in practical situations. Under these restrictions, allowed SU(3) rotations generate essentially only permutations of the hyperfine labels α and the corresponding chemical potentials μ_α. In the (μ_x,μ_y) plane, these permutations translate to C_3 rotations and reflections, and give a two-dimensional representation of the $\mathbb{S}_3 \sim C_{3v}$ group, implying a *triangular* symmetry of the phase diagram in this plane (see Fig. 3).

In addition to the symmetries discussed above, for an SU(3) symmetrical Hamiltonian, the mean-field equations also have a certain *particle-hole symmetry* if the single-particle density of states obeys $\varrho(\xi) = \varrho(-\xi)$, and the chemical potentials are set to a value $\mu \to \mu_{\mathrm{half}}$, such that ϱ is exactly half-filled. Under these conditions, we can show (see Appendix E) that the mean-field solutions are symmetrical in the sense that

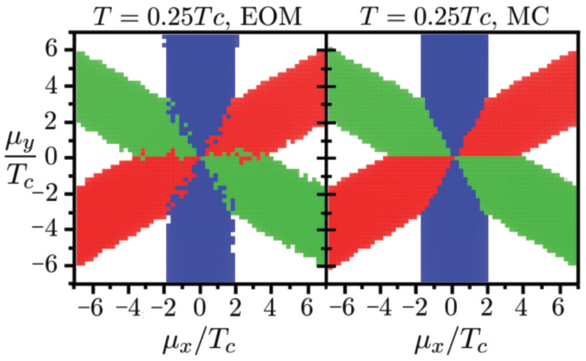

FIG. 5. (Color online) Comparison of the EOM and the Gaussian variational methods. Left: At low temperatures, the EOM equations have multiple solutions and become unreliable close to first-order phase boundaries. Right: The variational approach combined with a simulated annealing identifies correctly the physically relevant absolute minima of the free-energy density, Eq. (28). Parameters at the SU(3) symmetric point: $\lambda\,\rho_F = 0.112$, $\gamma W = 0.5$, $T_c/W = 0.011$, and $\xi_F/W = 0.24$ (half-filling).

for $\delta\mu_\alpha \equiv \mu_\alpha - \mu_{\rm half}$ and for $\delta\mu_\alpha \to -\delta\mu_\alpha$, the superfluid and magnetic symmetries are broken in the same channels and the order parameters are also equal apart from signs, global gauge transformations, and conjugation. In this special case, due to the additional permutational symmetry discussed above, the phase diagram exhibits a *sixfold* C_{6v} *symmetry* in the $(\delta\mu_x,\delta\mu_y)$ plane for traceless chemical potential shifts $\delta\mu_1 + \delta\mu_2 + \delta\mu_3 = 0$ (see Fig. 1.)

This particle-hole symmetry also emerges at the level of the Hamiltonian in certain cases. The half-filled attractive three-component Hubbard model on a bipartite lattice

$$H = -t \sum_\alpha \sum_{\langle ij\rangle} (a^\dagger_{i\alpha} a_{j\alpha} + \text{H.c.}) - \frac{U}{2} \sum_i \left(\sum_\alpha n_\alpha - \frac{3}{2} \right)^2,$$

e.g., has an exact particle-hole symmetry: it is invariant under the unitary transformation $a_{i\alpha} \leftrightarrow \text{sign}(i)\, a^\dagger_{i\alpha}$, with $\text{sign}(i)$ taking values ± for the two sublattices. Just as the mean-field symmetry discussed in the previous paragraph, this exact symmetry relates the order parameters of the symmetry broken phases for $\pm\delta\mu_\alpha$. We remark that, on a lattice, for stronger couplings, in addition to the SF/magnetic phases discussed here, other nontrivial phases may emerge (e.g., charge density waves or trionic phases).[16,25]

Although the particle-hole symmetry discussed here holds only for a single and special chemical potential value, we found that for $T_c \ll W$, higher-order terms in the Ginzburg-Landau action are only sensitive to the immediate vicinity of the Fermi surface. As a result, particle-hole symmetry becomes an *approximate symmetry* with a good accuracy whenever the slope of the single-particle density of states vanishes, $\gamma \equiv 0$. For SU(3) symmetric interactions and $\gamma \equiv 0$, we thus recover a phase diagram of hexagonal symmetry within our numerical accuracy (see Fig. 1).

III. MEAN-FIELD PHASE DIAGRAM

Let us now present the phase diagrams in the weak-coupling limit $T_c \ll W$, as obtained numerically, by the EOM and Monte Carlo methods presented in Sec. II.

A. Constant density of states ($\gamma = 0$)

As we argued in the Introduction, except for the SU(3) symmetric point, a system of constant DOS always favors the formation of a SF phase in one of the pairing channels (12), (23), and (31), having the smallest chemical potential difference. If the chemical potential difference between the components forming the SF state exceeds a certain limit (known as the Clogston limit[45] at zero temperature in case of two fermionic components), the system goes into the normal phase. This transition can either be of first or of second order, depending on the temperature.[23]

Figure 6 shows the numerically obtained phase diagram at different temperatures. All these cuts have the structure presented in Fig. 1. The hexagonal symmetry of the middle of the phase diagram is related to SU(3) symmetry: it is due to the invariance of the Hamiltonian under the permutations of the fermion species ($\alpha \leftrightarrow \beta$ and $\mu_\alpha \leftrightarrow \mu_\beta$) and the approximate particle-hole symmetry, as explained in Sec. II C.

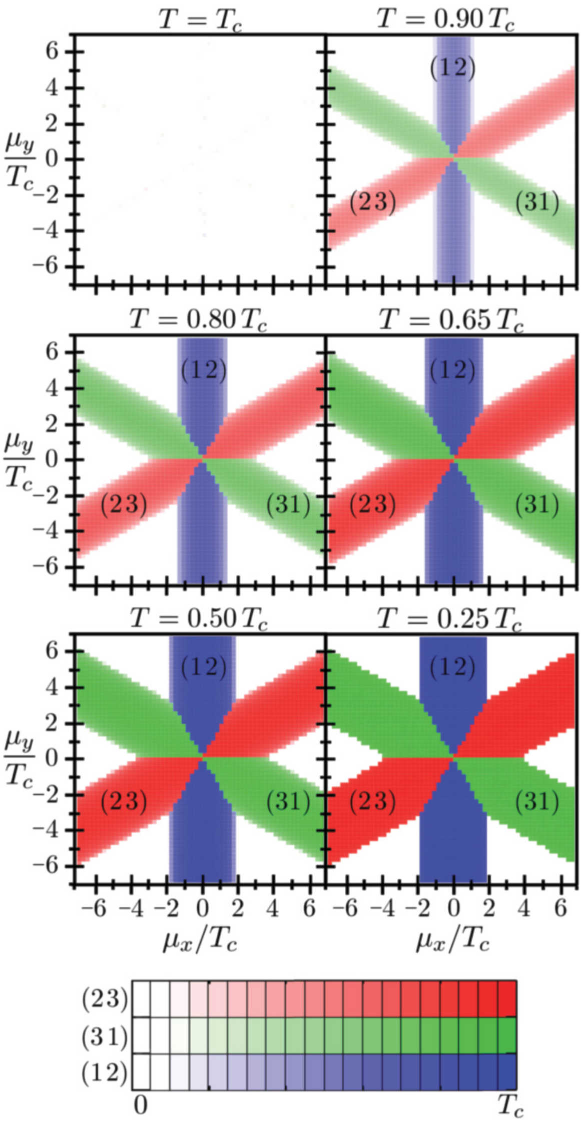

FIG. 6. (Color online) Mean-field phase diagrams at constant DOS, $\gamma = 0$. Different SF phases are separated by first-order lines. At $T = 0.25\,T_c$, SF-N transitions are of first order, whereas they become of second order for $T > \widetilde{T}^{\rm Sarma} \approx 0.48 T_c$ (see Sec. III C). Absolute values of components of the order parameter $\boldsymbol{\Delta}$ are given in units of T_c [see the respective color (gray) scales]. Parameters at the SU(3) symmetric point: $\lambda\,\rho_F = 0.1$, $T_c/W = 0.0076$, and $\gamma W = \xi_F/W = 0$.

The first-order SF-SF transitions appear along lines where the chemical potential differences between two different pairs of fermions become equal. Along some special directions in the (μ_x,μ_y) plane, two out of three fermions have equal chemical potentials, and can form a SF state even far away from the central SU(3) symmetric point. This explains the raylike structures in Fig. 6. In all other directions, the chemical potential differences continue to grow until the system goes into the normal phase at chemical potential differences of the order of the superfluid gap at the SU(3) symmetric point. For $T > \widetilde{T}^{\rm Sarma} \approx 0.48\,T_c$, this chemical potential driven SF-normal transition is of second order, however, it becomes of first order below $\widetilde{T}^{\rm Sarma}$ (see Sec. III C).

B. Linear density of states ($\gamma \neq 0$)

In the case of a nonconstant DOS ($\gamma \neq 0$), particle-hole symmetry is broken at the Fermi surface, and the SU(3) symmetrical point $\mu_x = \mu_y = 0$ is not invariant under the approximate particle-hole symmetry, either. At a first glance, the phase diagram is only slightly different from the $\gamma = 0$ case, however, at a closer look qualitative differences can be discovered (see bottom and top parts of Fig. 7). For $\gamma \neq 0$, the SF state does not necessarily form in the channel with the smallest chemical potential difference. The reason is that, as in standard BCS theory, the gap is exponentially sensitive to the DOS.[35] As a result, it may be favorable to form an SF state in channels where the DOS is larger at the chemical potential, even at the expense of Zeeman energy (chemical potential) loss. This mechanism is driven by the derivative of the DOS γ, and changes the phase diagram close to the SU(3) symmetric point. Here, the phase diagram has only threefold symmetry, corresponding to "color" permutations, and superfluidity forms in channels of the largest density of states. At higher values of the chemical potential, however, the phase diagram remains essentially unaltered, and is almost identical to that of constant density of states.

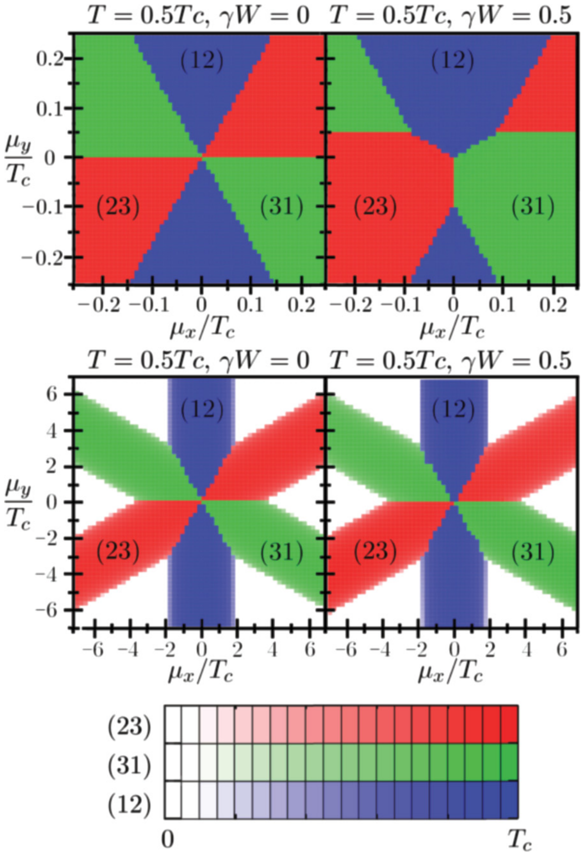

FIG. 7. (Color online) Phase diagrams at constant (left) and linear (right) DOS at $T = 0.5T_c$. Nonzero γ deforms the middle of the phase diagram (top right), whereas on the large scale (middle), the phase diagrams with constant and linear DOS are almost identical. For the absolute values of the SF order parameters, see the respective color (gray) scales. Parameters at the SU(3) symmetric point: $(\lambda\,\rho_F, T_c/W, \gamma W, \xi_F/W) = (0.1,0.0076,0,0)$ in the left and (0.112,0.011,0.5,0.24) in the right figures.

These results are similar to the predictions of Ref. [24], however, the phase structure differs somewhat, and the direction of the phase diagram of Ref. [24] seems to be flipped. We verified that both the variational calculation and the equation of motion method yield consistently the phase diagram presented here, which we can also reproduce by the Ginzburg-Landau approach, presented in Sec. IV. As we discuss there, the Ginzburg-Landau action of Ref. [24] can not produce the sixfold-symmetric structure of the overall phase diagram, and one needs to keep higher-order terms to recover it.

The previously discussed region of threefold symmetry is, however, usually small compared to the overall scale of the phase diagram. For the parameters of the left figures in Fig. 7, e.g., $T_c/W = 0.011$, and a relatively steep density of states with $\gamma W = 0.5$, the threefold-symmetric region is present only for $|\mu_x|,|\mu_y| < 0.1\ T_c$, while the overall scale of the phase diagram is about $\sim 3T_c$. The relative size of this central region increases for larger interaction strengths, and for $T_c/W = 0.105$ and $\gamma W = 0.5$, we find, e.g., that the central triangular region extends to $|\mu_x|,|\mu_y| < 0.25\ T_c$. The size of the central triangular region seems to scale roughly as $\sim\sqrt{\gamma T_c}$.

In Fig. 8, we confirm the predictions of Ref. [24] that breaking the SU(3) symmetry by the chemical potential can indeed lead to the appearance of superfluidity. Again, this is simply

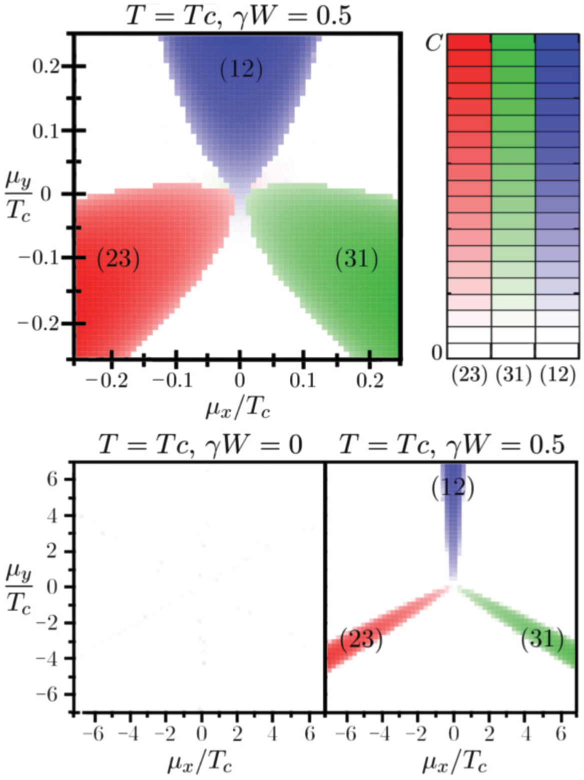

FIG. 8. (Color online) Phase diagrams at $T = T_c$ with constant (bottom left) and linear ($\gamma W = 0.5$) DOS (top left and bottom right). For linear DOS, the SF-N critical temperature can exceed T_c of the SU(3) symmetric point, whereas for $\gamma = 0$, the SF phase disappears everywhere above T_c. The largest values of the color (gray) scales correspond to $|\Delta_{\alpha\beta}| = 0.07T_c$ (top left) and $|\Delta_{\alpha\beta}| = T_c$ (bottom left and right). Parameters at the SU(3) symmetric point are $(\lambda\,\rho_F, T_c/W, \gamma W, \xi_F/W) = (0.1,0.0076,0,0)$ in the bottom left and (0.112,0.011,0.5,0.24) in the top left and bottom right figures.

related to the fact that the superfluid transition temperature is exponentially sensitive to the DOS at the Fermi energy. At the SU(3) critical temperature T_c, superfluidity appears only in small regions of the phase diagram, around the lines where two of the three fermion species have equal chemical potentials. These regions lie on that side of the SU(3) symmetric point, where the particles of the closest chemical potentials have higher DOS at the Fermi energy than the third one. We remark that the expansion of the free energy up to third order in the order parameters can not recover this structure precisely, and here the phase diagram is significantly different from the phase diagram of Ref. 24 (see Sec. IV for a more detailed discussion).

C. Two-component superfluidity

It is instructive to compare our mean-field theory with results obtained for two-component systems. As noticed by Sarma,[23] for two-component systems the Zeeman field-induced SF-N transition becomes of first order below the temperature T^{Sarma}, and above the chemical potential difference $\mu_x^{\text{Sarma}} = (\mu_1^{\text{Sarma}} - \mu_2^{\text{Sarma}})/\sqrt{2}$. Sarma also determined the mean-field values of this critical point (Sarma point), and obtained

$$T^{\text{Sarma}} = 0.58\, T_c\ , \quad \mu_x^{\text{Sarma}} = 1.5\, T_c\ , \tag{33}$$

with T_c the critical temperature at $\mu_x = 0$. He also determined the critical chemical potential difference at zero temperature, known as the Clogston limit[45]:

$$\mu_x^{\text{Clog}} = 2\,\Delta(T=0) = 1.764\, T_c\ , \tag{34}$$

with Δ denoting the SF order parameter.

The three-component system exhibits a two-component behavior in regimes where the chemical potential of two species remains close, e.g., $|\mu_1 - \mu_2| \sim T_c$, while that of the third component is very far from them ($|\mu_3| \gg T_c$). To investigate this limit, we fixed $\mu_y = 5T_c$, and varied μ_x, along the solid line shown in the top left panel of Fig. 9. The corresponding SF phase diagram displays features similar to those predicted by Sarma. At $T = 0$ temperature, the absolute value of the SF order parameter is independent of μ_x in the superfluid phase, and its magnitude agrees with the BCS result $\Delta(T=0) = 0.882\, T_c^{(*)}$, with $T_c^{(*)}$ being the critical temperature at $\mu_x = 0$.[46] The critical value of μ_x (Clogston limit), however, shows significant deviations compared to Eq. (34). For a coupling $\tilde{\lambda} \equiv \lambda\rho_F = 0.1$, e.g., we find both for a two- *and* for a three-component system:

$$\mu_x^{\text{Clog}} \to \widetilde{\mu}_x^{\text{Clog}}|_{\tilde{\lambda}=0.1} = 2.19\,\Delta(T=0) = 1.93\, T_c^{(*)}\ . \tag{35}$$

For $T_c \ll W$, the prefactor was found to be approximately independent of the value of μ_y and particle-hole symmetry-breaking parameter $\tilde{\gamma}$. The difference between Eq. (35) and Clogston's result is due to the inclusion of magnetic degrees of freedom in the free-energy density, Eq. (28), which accounts for interaction-related contributions to the Pauli susceptibility $\chi \sim \rho_F$, neglected in Sarma's work.[23] These susceptibility contributions are proportional to $\lambda_{\alpha\beta}\rho_F^2$, and therefore result in a correction to the magnetic energy of relative size $\sim\lambda_{12}\rho_F$, in rough agreement with the numerically observed shift of μ_x^{Clog}. It is easy to understand this difference on physical grounds: In the SF state (12), the densities n_{11} and n_{22} are exactly equal at $T = 0$, while in the normal state they shift according to the chemical potential difference. The interaction is, however, repulsive in the magnetic channel. Consequently, the (magnetized) normal state becomes less favorable, and μ_x^{Clog} shifts upwards.

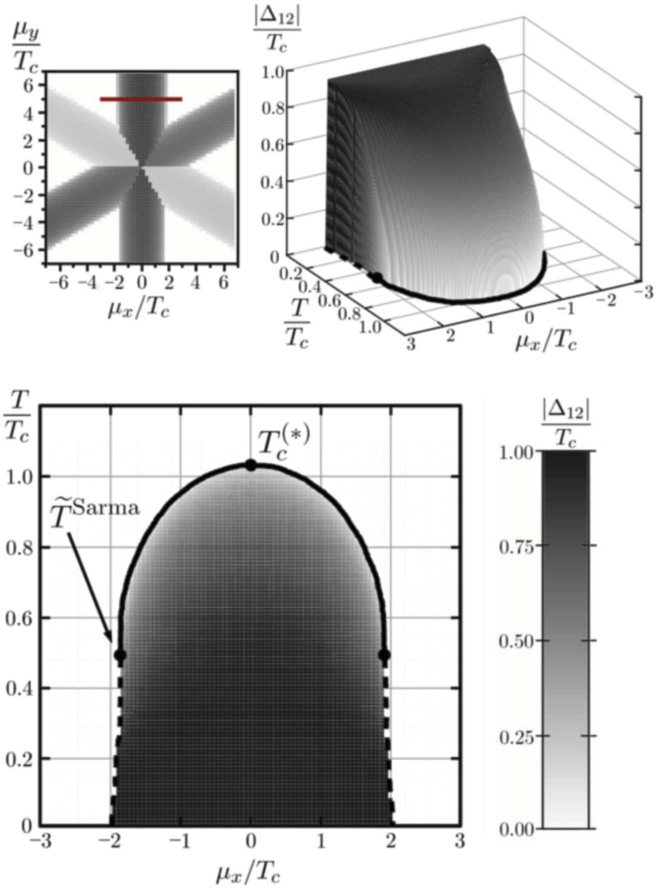

FIG. 9. (Color online) SF phase diagram (top right and bottom) at linear DOS ($\gamma W = 0.5$), with $\mu_y = 5T_c$ kept constant, as indicated by the solid line in the top left figure. The SF-N transition becomes from second order (solid line) to first order (dashed line) below the temperature $\widetilde{T}^{\text{Sarma}} = 0.48\, T_c^{(*)}$, and chemical potential difference $\widetilde{\mu}_x^{\text{Sarma}} = 1.842\, T_c^{(*)}$, with $T_c^{(*)} = 1.027\, T_c$ the critical temperature at $\mu_x = 0$ and $\mu_y = 5T_c$. Parameters at the SU(3) symmetric point were $\lambda\,\rho_F = 0.1, \gamma W = 0.5, T_c/W = 0.0076, \xi_F = 0$.

Locating numerically the Sarma point we also find that it is shifted compared to Eq. (33):

$$T^{\text{Sarma}} \to \widetilde{T}^{\ \text{Sarma}}|_{\tilde{\lambda}=0.1} = 0.48\, T_c^{(*)}\ , \tag{36}$$

$$\mu_x^{\text{Sarma}} \to \widetilde{\mu}_x^{\ \text{Sarma}}|_{\tilde{\lambda}=0.1} = 1.842\, T_c^{(*)}\ , \tag{37}$$

again, approximately independently from the value of γ. These results and Eq. (35) demonstrate that the positions of the Sarma point and the Clogston point [Eq. (34)] can significantly deviate from their standard BCS values due to interaction effects. Furthermore, their independence from the particular value of γ shows that, at least for $T_c \ll W$, particle-hole symmetry breaking does not have a significant effect on the SF phases in the regime where the chemical potentials are far from the SU(3) symmetric point.

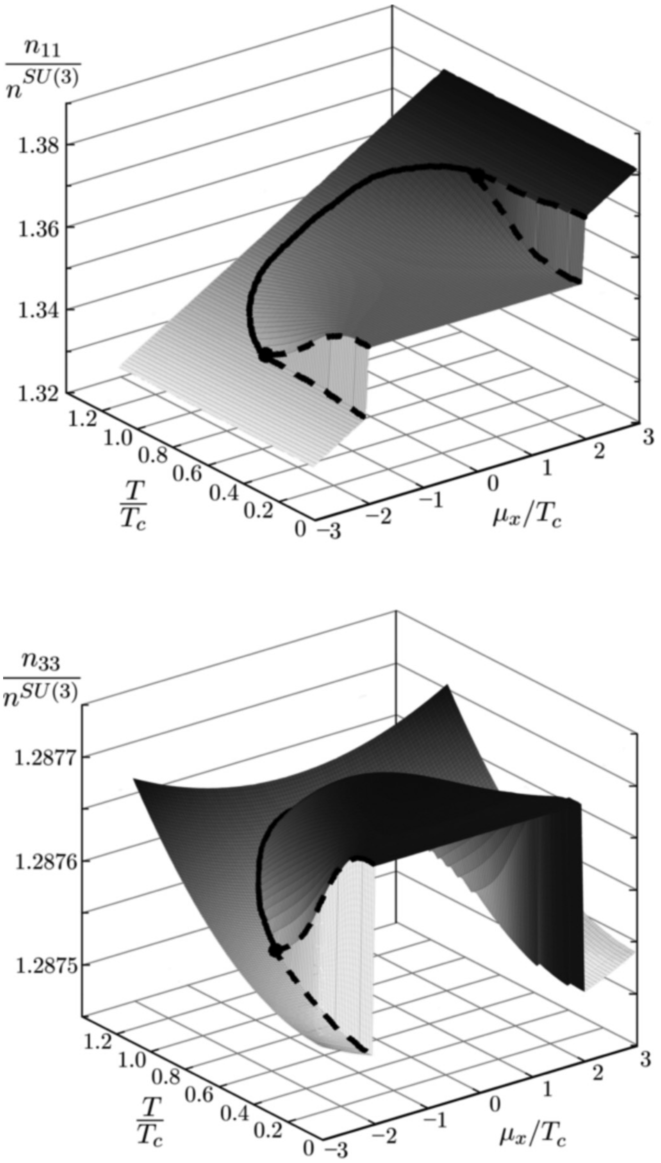

FIG. 10. Interplay between superfluidity and magnetism in the SF channels, $\alpha = 1,2$ (top), and for the third, normal component (bottom), for linear DOS ($\gamma W = 0.5$), with $\mu_y = 5T_c$ kept constant. The shift of the densities along the SF-N phase boundary is smooth for $T > \widetilde{T}^{\text{Sarma}}$ (solid line), and discontinuous for $T < \widetilde{T}^{\text{Sarma}}$ (dashed line). The density jump of the third component is much smaller than that of the SF components. (See also Fig. 9.) Parameters at the SU(3) symmetric point: $\lambda\rho_F = 0.1, \gamma W = 0.5, T_c/W = 0.0076, \xi_F = 0$.

In the SF state, the SF species are bound together, and the condensate itself can not be polarized. This has an experimentally important manifestation at the SF-N transition, where a sudden shift appears in the densities at the phase boundary, as presented in Fig. 10. At zero temperature, the densities in the SF channel are equal, and their value does not depend on the chemical potential difference, whereas at the SF-N transition, a difference in the densities sets in. At temperatures below $\widetilde{T}^{\text{Sarma}}$, the SF-N transition is of first order, and the densities jump discontinuously on the phase boundary. In Fig. 10, this amounts to a ∼1% jump in the densities. In the strongly interacting regime, however, the jump is expected to take much higher values, similar to two-component systems.[8]

Let us close this section by investigating the effect of SF transition on the third, normal component. Indeed, in the presence of particle-hole symmetry breaking, the SF order parameter couples directly to the magnetization, and should shift the density of the third component. Figure 10 shows this effect for a linear DOS in the weak-coupling limit. We find that the shift in the density of the third component is only of the order of 0.01% for $T_c/W = 0.0076$, however, for larger ratios $T_c/W = 0.1$ (but the same γ), it reaches values of the order of 1%, indicating that this effect may be measurable in the strong-coupling regime.[47]

IV. GINZBURG-LANDAU ACTION

In this section, we focus on the central region of the phase diagram, and construct a Ginzburg-Landau (GL) expansion of the free energy (28) around the SU(3) symmetric point $\mu_x = \mu_y = 0$ for $T \approx T_c$. Throughout this section, we assume a perfectly SU(3) symmetrical interaction $\lambda_{\alpha\beta} = \lambda$ for $\alpha \neq \beta$. While the form of the Ginzburg-Landau functional is dictated by symmetry, the coefficients of the various terms depend on the microscopic parameters. We shall give approximate expressions for them, as obtained through a numerical analysis of Eq. (28).

In the weak-coupling limit, the dimensionless free-energy density

$$\widetilde{f}_G \equiv f_G/\left(\rho_F T_c^2\right)$$

can only depend on a few dimensionless physical parameters: the dimensionless interaction $\widetilde{\lambda} \equiv \rho_F \lambda$, the dimensionless slope of the DOS at the Fermi energy $\widetilde{\gamma} \equiv \gamma T_c$, the reduced temperature $t \equiv (T - T_c)/T_c$, and the dimensionless chemical potential differences $\delta\widetilde{\mu} = (\mu - \mu^{\text{SU(3)}})/T_c$, with $\mu^{\text{SU(3)}}$ denoting the chemical potential at the SU(3) symmetric point.[48] Most importantly, however, $\widetilde{f}_G$ is a functional of the dimensionless order parameters

$$\widetilde{\boldsymbol{\Delta}} \equiv \boldsymbol{\Delta}/T_c\,, \quad \delta\widetilde{\boldsymbol{\Lambda}} \equiv (\boldsymbol{\Lambda} - \boldsymbol{\Lambda}^{\text{SU(3)}})/T_c\,, \tag{38}$$

with $\boldsymbol{\Lambda}^{\text{SU(3)}}$ denoting the renormalized chemical potential at the SU(3) symmetric point.

The expansion of the free energy contains only SU(3) invariant terms and can therefore be expanded as[24]

$$\begin{aligned} \widetilde{f}_G = {} & A_1\,\text{Tr}(\widetilde{\boldsymbol{\Delta}}\widetilde{\boldsymbol{\Delta}}^+) + A_2\,\text{Tr}[(\widetilde{\boldsymbol{\Delta}}\widetilde{\boldsymbol{\Delta}}^+)^2] \\ & + B_1\,\text{Tr}(\delta\widetilde{\boldsymbol{\Lambda}}^2) + B_2\,\text{Tr}(\delta\widetilde{\boldsymbol{\Lambda}})^2 + B_3\,\text{Tr}(\delta\widetilde{\boldsymbol{\mu}}\,\delta\widetilde{\boldsymbol{\Lambda}}) \\ & + C_1\,\text{Tr}(\delta\widetilde{\boldsymbol{\Lambda}}\widetilde{\boldsymbol{\Delta}}\widetilde{\boldsymbol{\Delta}}^+) + C_2\,\text{Tr}(\delta\widetilde{\boldsymbol{\Lambda}})\text{Tr}(\widetilde{\boldsymbol{\Delta}}\widetilde{\boldsymbol{\Delta}}^+) \\ & + C_3\,\text{Tr}(\delta\widetilde{\boldsymbol{\mu}}\widetilde{\boldsymbol{\Delta}}\widetilde{\boldsymbol{\Delta}}^+) + \cdots . \end{aligned} \tag{39}$$

The eight coefficients appearing in this expansion are all functions of $\widetilde{\lambda}$, t, and $\widetilde{\gamma}$. We determined them by fitting the free energy Eq. (28) numerically, and found that the expressions in Table I give a good estimate for these parameters.[49] At the minima of the free-energy functional above, we have $\delta\widetilde{\boldsymbol{\Lambda}} \propto \delta\widetilde{\boldsymbol{\mu}}$ and $\widetilde{\boldsymbol{\Delta}} \propto \sqrt{t}$. Therefore, the expansion above contains all terms up to $\mathcal{O}(t^2, \delta\widetilde{\mu}\,t, \delta\widetilde{\mu}^2)$.

The superfluid phase transition is driven by the term $A_1(t,\widetilde{\lambda})$, which changes sign at the SU(3) point. All other

TABLE I. Approximate expressions of the Ginzburg-Landau coefficients in Eq. (39). The dimensionless parameters are $\widetilde{\lambda} \equiv \rho_F \lambda$, $\widetilde{\gamma} \equiv \gamma T_c$, and $t \equiv (T - T_c)/T_c$.

Parameter	Approximate expression
A_1	$2.00\,t + \cdots$
A_2	$0.40 - 1.20t + \cdots$
B_1	$0.5000 + 1.000\,\widetilde{\lambda} + \cdots$
B_2	$-1.000\,\widetilde{\lambda} + \cdots$
B_3	$-1.000 + \cdots$
C_1	$1.25\,\widetilde{\gamma} + \cdots$
C_2	$-1.22\,\widetilde{\gamma} + \cdots$
C_3	$-0.62\,\widetilde{\gamma}/\widetilde{\lambda} + \cdots$

TABLE II. Approximate expressions of the Ginzburg-Landau coefficients in Eq. (40). The dimensionless parameters are $\widetilde{\lambda} \equiv \rho_F \lambda$, $\widetilde{\gamma} \equiv \gamma T_c$, and $t \equiv (T - T_c)/T_c$.

Parameter	Approximate expression
a_1	$2.0\,t + \cdots$
a_2	$0.40 - 1.2\,t + \cdots$
b	$(3.2\,t - 0.083/\widetilde{\lambda}^2)\,\widetilde{\gamma} + \cdots$
c_1	$0.125 - 0.29\,\widetilde{\lambda} - 0.13\,t + \cdots$
c_2	$-0.115 + 0.27\,\widetilde{\lambda} + 0.12\,t + \cdots$

coefficients are approximately constant close to the phase transition. The terms $\sim B_i$ describe the ferromagnetic order parameter and its response to the external "magnetic field" $\widetilde{\mu}$. The most interesting terms are those proportional to the coefficients C_i: these describe the coupling between the SF order parameter and the magnetization (or chemical potential differences), and they are responsible for the threefold-symmetric structure in the central region of the phase diagram (see Fig. 7). The terms C_1 and C_2 couple the superfluid and magnetic order parameters, and produce the density shift of the normal component at the onset of superfluidity. Notice that all these terms are found to be proportional to the dimensionless particle-hole symmetry-breaking parameter $\widetilde{\gamma}$.

While the third-order expansion (39) accounts for the central regions in the right panels of Fig. 7, it does not recover the sixfold-symmetric structure that dominates the phase diagram at larger chemical potential differences. This is obvious since the terms C_1, C_2, and C_3 are odd under the particle-hole transformation $\delta\widetilde{\mu} \leftrightarrow -\delta\widetilde{\mu}$, $\delta\widetilde{\mathbf{\Lambda}} \leftrightarrow -\delta\widetilde{\mathbf{\Lambda}}^*$, and are proportional to γ, while the hexagonal structure is even under particle-hole transformation, and already appears for $\gamma = 0$. The "hexagonal" structure must therefore be controlled by higher-order terms, containing even degree polynomials of $\delta\widetilde{\mu}$ and $\delta\widetilde{\mathbf{\Lambda}}$, coupled to the SF order parameter. Unfortunately, the number of such terms is huge, and is next to impossible to determine all of them and their corresponding GL coefficients accurately. However, observing that the ferromagnetic response is always small, we can just focus on the SF order parameter. At a formal level, this can be done by minimizing the free-energy functional $\widetilde{f}_G$ in $\delta\widetilde{\mathbf{\Lambda}}$ for any fixed $\delta\widetilde{\boldsymbol{\mu}}$ and $\widetilde{\mathbf{\Delta}}$, and thus defining

$$\widehat{f}_G(\delta\widetilde{\boldsymbol{\mu}},\delta\widetilde{\mathbf{\Delta}}) \equiv \widetilde{f}_G(\delta\widetilde{\boldsymbol{\mu}},\delta\widetilde{\mathbf{\Delta}},\delta\widetilde{\mathbf{\Lambda}}_{\min}(\delta\widetilde{\boldsymbol{\mu}},\delta\widetilde{\mathbf{\Delta}})).$$

The form of this GL functional is also dictated by symmetry, and it can also be expanded in $\delta\widetilde{\boldsymbol{\mu}}$ and $\delta\widetilde{\mathbf{\Delta}}$. Up to $\mathcal{O}(t^2,\delta\widetilde{\mu}^2\,t)$, it reads as[49]

$$\widehat{f}_G = a_1\,\mathrm{Tr}(\widetilde{\mathbf{\Delta}}\widetilde{\mathbf{\Delta}}^+) + a_2\,\mathrm{Tr}[(\widetilde{\mathbf{\Delta}}\widetilde{\mathbf{\Delta}}^+)^2] + b\,\mathrm{Tr}(\delta\widetilde{\boldsymbol{\mu}}\widetilde{\mathbf{\Delta}}\widetilde{\mathbf{\Delta}}^+) + c_1\,\mathrm{Tr}(\delta\widetilde{\boldsymbol{\mu}}^2\widetilde{\mathbf{\Delta}}\widetilde{\mathbf{\Delta}}^+) + c_2\,\mathrm{Tr}(\delta\widetilde{\boldsymbol{\mu}}\widetilde{\mathbf{\Delta}}\delta\widetilde{\boldsymbol{\mu}}\widetilde{\mathbf{\Delta}}^+) + \cdots . \tag{40}$$

The approximate values of the numerically obtained coefficients are enumerated in Table II.

Minimization of Eq. (40) yields the correct structure of the phase diagram in the vicinity of the SU(3) symmetric point, and accounts for the competition between the odd $(b,\ldots)$ and even $(c_1,c_2,\ldots)$ order couplings. We also checked that it determines correctly the absolute value of the SF order parameter in the weak-coupling regime $T_c/W < 0.1$ at temperatures $0.9T_c < T < T_c$. However, the locations of the triple points at the interface of the threefold- and approximately sixfold-symmetric structures in Fig. 7 are reproduced only with an error of about 50%. Although this error is very large, it is also natural, since on the scale of this structure, the chemical potential difference is of the order of $\delta\widetilde{\mu} \approx 0.2$. Therefore, $\delta\widetilde{\mu}$ can not be considered as a small parameter here, and higher-order terms in the expansion (40) shift the phase boundaries significantly.

V. BEYOND MEAN-FIELD

In the discussion presented so far, we restricted ourselves to a mean-field approach, and neglected fluctuations. Fluctuations, however, not only reduce somewhat the transition temperatures and fields, but they also change the universality class and thus the critical exponents of the transition. In ordinary superfluids, such fluctuation effects are typically hard to observe, however, in cold-atomic systems one can reach the strong-coupling regime, and therefore a nontrivial critical behavior may be observable.[50]

First, let us discuss the central SU(3) symmetrical point of the phase diagram $\mu_x = \mu_y = 0$. At this point, only the first two terms of the GL action (40) survive for an SU(3) symmetrical interaction. These terms as well as the gradient term $\mathrm{Tr}\{\partial_{\mathbf{r}}\mathbf{\Delta} \cdot \partial_{\mathbf{r}}\mathbf{\Delta}^+\}$ have an increased O(6) symmetry with respect to SU(3),[49] with the real and imaginary parts of the independent components of $\mathbf{\Delta}$ forming a six-component real vector. Since higher-order terms are irrelevant in the renormalization group (RG) sense, the $\mu_x = \mu_y = 0$ transition is described by the O(6) critical theory. Thus, the correlation length diverges as $\xi \sim |T - T_c|^{-\nu_{O(6)}}$, while the order parameter scales as $\langle \mathbf{\Delta} \rangle \sim |T - T_c|^{\beta_{O(6)}}$. For $d = 3$ dimensions, the critical exponents are known from ϵ expansions,[51] $1/n$ expansions,[52] as well as from high-temperature expansions,[53] and Monte Carlo simulations,[54] giving similar results

$$\nu_{O(6)}^{3D} \approx 0.80, \quad \beta_{O(6)}^{3D} \approx 0.41 .$$

In two dimensions, on the other hand, fluctuations suppress the phase transition at the SU(3) symmetrical point $T_c^{2D} \to 0$,[55] which thus becomes a quantum critical point.

For generic values of $\mu_x,\mu_y \neq 0$, only one superfluid channel dominates the phase transition, which is therefore described by the XY model. In $d = 3$ dimensions, the corresponding critical exponents are given by[56]

$$\nu_{XY}^{3D} \approx 0.67, \quad \beta_{XY}^{3D} \approx 0.35, \tag{41}$$

while in $d = 2$ dimensions the transition is of Kosterlitz-Thouless type.[57]

Interesting critical behavior emerges in the vicinity of the bicritical lines of Fig. 2. Along these lines, two components of the matrix $\mathbf{\Delta}$, e.g., Δ_{13} and Δ_{23} compete with each other to form the superfluid. These can be grouped into a real four-component vector $\varphi = (\mathrm{Re}\Delta_{23},\mathrm{Im}\Delta_{23},\mathrm{Re}\Delta_{13},\mathrm{Im}\Delta_{13})$. Fermion number conservation implies that the effective action must be invariant under global phase transformations $\Delta_{ij} \to e^{i\phi_{ij}}\Delta_{ij}$, which translates to an O(2) × O(2) symmetry in terms of the field φ. Up to fourth order, the most general effective Hamiltonian can be written as[58]

$$H_{LW} = \int d^dx \left[\frac{1}{2}(\nabla\varphi)^2 + t_+\varphi^2 + t_-\varphi\mathbf{\Pi}\varphi \right.$$
$$\left. + u(\varphi^2)^2 + v(\varphi\mathbf{\Pi}\varphi)^2 + w\varphi^2(\varphi\mathbf{\Pi}\varphi) + \cdots \right], \quad (42)$$

where the terms breaking the O(4) symmetry were written in terms of the matrix

$$\mathbf{\Pi} = \begin{pmatrix} 1 & & & \\ & 1 & & \\ & & -1 & \\ & & & -1 \end{pmatrix}. \quad (43)$$

In the absence of the terms t_- and w, this action has an additional $\mathbb{Z}_2$ symmetry $\Delta_{13} \leftrightarrow \Delta_{23}$, leading to a $\mathrm{O}(2,2) = (\mathrm{O}(2)\times\mathrm{O}(2)) \rtimes \mathbb{Z}_2$ symmetry of the free-energy functional. In the presence of particle-hole symmetry, one can show that at the boundary of the two superfluid phases, the $\mathbb{Z}_2$ violating terms vanish: $t_- = w = 0$. In general, however, the simultaneous vanishing of t_- and w is not guaranteed. Nevertheless, already leading-order ϵ expansion indicates[59] that the coupling w is irrelevant at the phase transition $t_\pm \to 0$. Thus, the $\mathbb{Z}_2$ symmetry is apparently restored at the transition, and the critical state must be described by the O(2,2) symmetrical functional with $t_-, w \to 0$.

The O(2,2) functional (42) with $t_-, w \to 0$ thus describes the phase transition at all bicritical endpoints where two superfluid phases meet (white circles in Fig. 11). Notice that the structure of the phase diagram changes close to T_c, and the six O(2,2) points, characteristic at lower temperatures, pairwise merge into three O(2,2) points above a tricritical temperature T^{tri} (as also shown in Fig. 11).

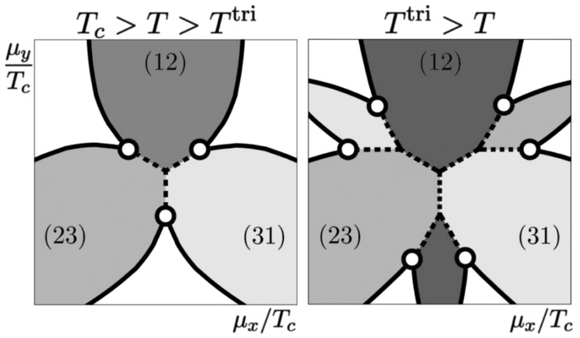

FIG. 11. Schematic picture of the position of the O(2,2) points (empty circles) in case of linear DOS. At the temperature T^{tri} below which the triple points appear, from each O(2,2) bicritical line (left) two new bicritical lines of the same universality class branch out (right). The branching points are multicritical. SF-SF transitions are of first order (dashed lines), whereas SF-N transitions are of second order (solid lines).

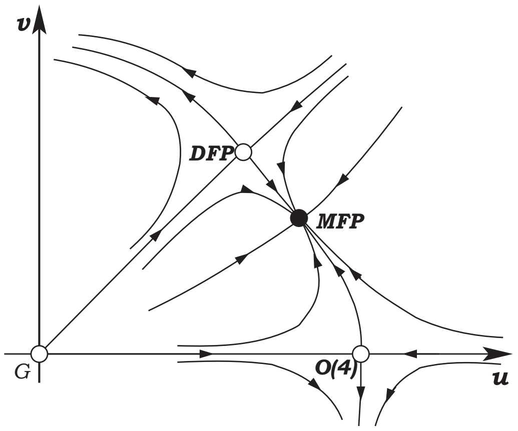

FIG. 12. Schematic picture of the $\mathcal{O}(\epsilon^2)$ RG flows in the (u,v) plane, with $t_- = w = 0$, for $\epsilon < 5/7$. For $\epsilon \to 1$, the fixed-point structure changes, and the ϵ expansion is inconclusive.

The second-order terms t_+ and t_- trigger the SF-N and SF-SF transitions, respectively, and scale as

$$t_+ \propto \delta\mu_\parallel, \quad (44)$$

$$t_- \propto \delta\mu_\perp \quad (45)$$

for small chemical potential shifts parallel $(\delta\mu_\parallel)$ and perpendicular $(\delta\mu_\perp)$ to the SF-SF phase boundary.

The model (42) has been studied extensively,[59,60] typically in the framework of the more general $n\cdot m$ component models.[61] Despite the extensive effort, the stability of its various fixed points is still debated. Systematic ϵ expansion yields three nontrivial fixed points with $t_\pm^* = w^* = 0$, which could potentially describe the critical state: (a) an O(4) Heisenberg fixed point with $u^* > 0$ and $v^* = w^* = 0$, (b) a decoupled fixed point (DFP) $(u^* = v^*, w^* = 0)$, where the two superfluid components are described by two independent XY theories, and (c) a mixed (or biconical) fixed point (MFP) with $u^* \neq v^*$ and $w^* = 0$.

For small values of $\epsilon = 4 - d$, ϵ expansion yields the picture shown in Fig. 12, predicting that the mixed fixed point (MFP) describes the phase transition along the O(2,2) critical line. However, already in second order in ϵ,[62] the fixed-point structure changes completely as one approaches the physical value $\epsilon = 1$, and even the results of six loop ϵ expansion remain completely inconclusive regarding the stability of the fixed points.[63] Nonperturbative arguments, on the other hand, seem to support that the rather boring decoupled fixed point (DFP) describes the critical state.[63–65]

The universality class of the fixed point has considerable impact on the phase diagram. The ratio of the critical exponents $y_\pm$ associated with the terms $t_\pm$ determine, e.g., the shape of the SF-N phase boundary in the vicinity of the bicritical point. Standard crossover scaling arguments[55] lead to the conclusion, e.g., that the specific heat diverges in the vicinity of the SF-N transition line as

$$c_v(t_+) \propto |t_+ - C(t_-)|^{-\alpha_{XY}}, \quad (46)$$

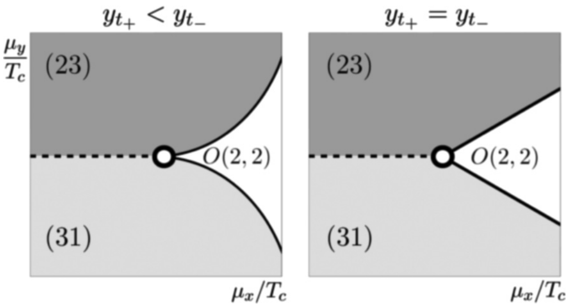

FIG. 13. Schematic phase diagram of the vicinity of the O(2,2) bicritical point (see Fig. 1) in case of the mixed (left) and the decoupled (right) fixed point. In the former case, fluctuations modify the SF-N phase boundary into curves with universal scaling.

where α_{XY} denotes the specific-heat exponent of the XY model, and the phase boundary is determined by the function $C(t_-)$:

$$C(t_-) \propto |t_-|^{y_+/y_-}. \tag{47}$$

Since the critical exponents $y_\pm$ are different for the two possible stable fixed points even to first order in ϵ,

$$y_+^{\mathrm{MFP}} = 2 - \epsilon/2 + \cdots, \quad y_-^{\mathrm{MFP}} = 2 - \epsilon/6 + \cdots,$$
$$y_\pm^{\mathrm{DFP}} = 2 - \tfrac{2}{5}\epsilon + \cdots, \tag{48}$$

the shape of the phase boundary will be different in the two cases. Notice that since the DFP describes two independent XY models, its exponents $y_\pm^{\mathrm{DFP}}$ will be equal to all orders in ϵ, implying that the SF-N boundaries start *linearly* at the bicritical point. For the MFP, on the other hand, $y_+^{\mathrm{MFP}} < y_-^{\mathrm{MFP}}$, and the SF-N boundary has a universal exponent in the vicinity of the O(2,2) point, as shown in Fig. 13. This difference in the shape of the phase boundary provides a clear fingerprint of the universality class of the transition.

The critical exponent β of the order parameter $\langle\varphi\rangle$ along the SF-SF phase boundary is determined by the exponent y_h of the "magnetic field" at the critical fixed point

$$\beta = \frac{d - y_h}{y_+}. \tag{49}$$

Since the magnetic field exponents get their first nontrivial contribution in $\mathcal{O}(\epsilon^2)$ order, to leading order in ϵ we have

$$y_h^{\mathrm{DFP}} = 3 - \frac{\epsilon}{2} + \cdots; , \quad y_h^{\mathrm{MFP}} = 3 - \frac{\epsilon}{2} + \cdots. \tag{49}$$

However, since $y_+^{\mathrm{MFP}} \neq y_+^{\mathrm{DFP}}$, the exponents β^{DFP} and β^{MFP} turn out to be different already to first order in ϵ,

$$\beta^{\mathrm{DFP}} = \frac{1}{2} - \frac{3}{20}\epsilon + \cdots, \quad \beta^{\mathrm{MFP}} = \frac{1}{2} - \frac{\epsilon}{8} + \cdots. \tag{50}$$

VI. EXPERIMENTAL RELEVANCE

Currently, maybe ^{6}Li ultracold gases provide the most promising perspective for the realization of three-component superfluidity. For high magnetic fields, the s-wave scattering lengths between the three lowest hyperfine states approach the spin-triplet scattering length $a_{12} \approx a_{23} \approx a_{31} \approx -2140\, a_0$, with a_0 the Bohr radius.[27] At fields of ~2000 G, for example, the scattering lengths all deviate less than 2% from their average value.[27] It has been proposed theoretically that this deviation can further be decreased using radiofrequency (rf) and microwave fields (mw),[28] down to 0.1 %, and thereby a strongly attractive system can be realized with almost perfect SU(3) symmetry in this high-field regime.

Although three-body loss is a major obstacle in three-component experiments, recent experiments showed that decay rates tend to decrease at high fields in ^{6}Li systems, and indeed, Fermi degeneracy has successfully been realized in this three-component system.[17] According to our estimate, a ^{6}Li experiment in the high magnetic field limit on a system of Fermi energy $T_F = 1\ \mu$K and without optical lattice would correspond to the parameters $\lambda_{\alpha\beta}\, \rho_F \approx 0.11, \gamma W \approx 0.18$, and $T_c/W \approx 0.01$.[66] This system would thus be in the regime of weak interactions, studied here. However, such a small critical temperature is currently unreachable. Application of an optical lattice can, however, easily bring the system into the regime of strong interactions, where SU(3) superfluidity may be accessible.[68] Although our calculations do not apply for strong interactions, we believe that, similar to the SU(2) case,[5,6,8,23] the major features of our phase diagram are robust, and should carry over to the strongly interacting case.[25,40]

So far, we assumed a perfectly SU(3) symmetrical interaction in our calculations. The phase diagram is, however, somewhat modified if the the scattering lengths are only approximately equal.[69,70] In Fig. 14, we present a phase diagram for the case where we have set the ratio of critical temperatures in the different channels to be $T_c^{(23)}/T_c^{(12)} = T_c^{(31)}/T_c^{(12)} = 0.95$. For $T_c^{(ij)}/W \sim 0.01$, this would correspond to a ~1% asymmetry of the scattering lengths. At temperatures $T_c^{(12)} > T > T_c^{(23)} = T_c^{(31)}$, the SF phase is formed only in the (12) channel. The starlike shape of the phase diagram is preserved at lower temperatures, however, the interaction asymmetry destroys the sixfold symmetry of the central region of the phase diagram, including the O(6) critical point: the phase (12) dominates this central region and expels the other two SF phases. Thus, the shape of this region depends rather sensitively on the interaction asymmetry, and fine tuning of the scattering lengths (by using rf and mw fields,[28] e.g.) may be needed to realize an SU(3) symmetric superfluid.

VII. CONCLUSIONS

In this paper, we studied the phase diagram and the interplay of fermionic and superfluid order parameters in a three-component fermionic mixture. We mostly focused on the case of SU(3) symmetrical interactions and studied the weak-coupling regime, where the critical temperature is much smaller than the Fermi energy of the atoms, $T_c \ll E_F \sim W$.[71] We combined two complementary mean-field methods (Gaussian variational method and equation of motion techniques) to study how a chemical potential imbalance polarizes the atomic cloud and modifies/destroys superfluid order. Although the phase diagram of the three-component system is naturally much richer than that of the two component mixture,[23] there are some similarities: large chemical potential imbalances ($|\mu_i - \mu_j| \gg T_c$ for all $i \neq j$), for example, destroy superfluid (SF) order, similar to two-component mixtures. The corresponding

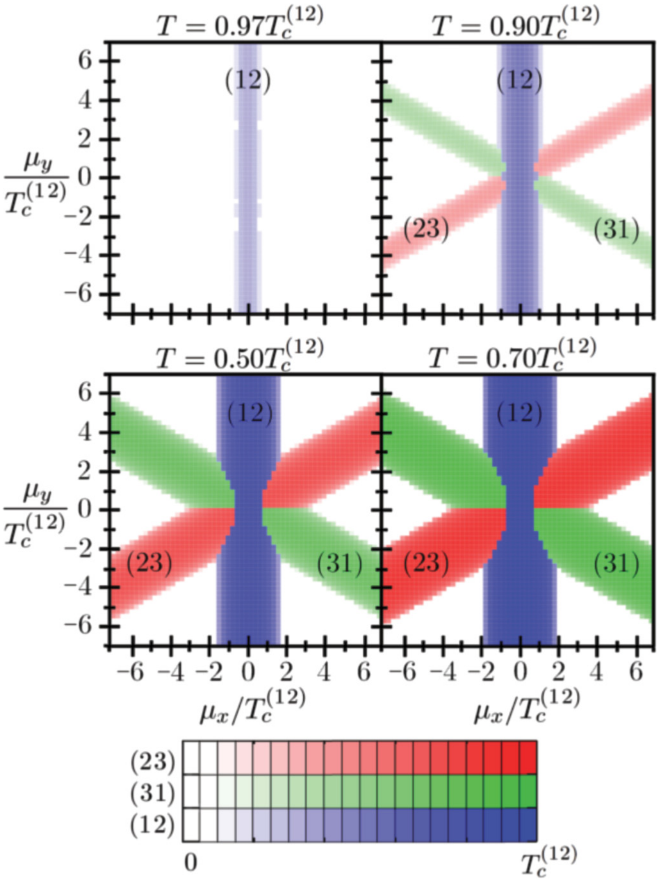

FIG. 14. (Color online) Phase diagram with only approximately equal interaction strengths. The rate of the critical temperatures in the respective channels are $T_c^{(23)}/T_c^{(12)} = T_c^{(31)}/T_c^{(12)} = 0.95$. The SF phase in the channel of strongest interaction repels the other two phases from the central region of the phase diagram. See the respective color (gray) scales for the absolute values of the SF order parameters. Parameters at the $\mu_x = \mu_y = 0$ point: $(\lambda_{12},\lambda_{23},\lambda_{31})\rho_F = (0.1057,0.1046,0.1046), T_c^{(12)}W = 0.01, \gamma W = 0, \xi_F = 0$.

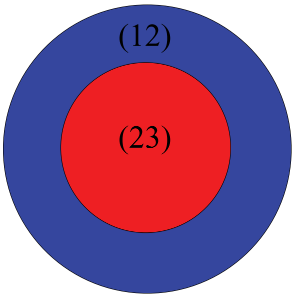

FIG. 15. (Color online) Possible trap configurations for total atom numbers $N_3 > N_2 \gtrsim N_1$.

SF-normal transition is of second order at higher temperatures, while it becomes of first order below the Sarma temperature.

The superfluid phase is, on the other hand, much richer than in the two-component case. SF order can form in channels (12), (23), and (31), and the chemical-potential-driven transitions between these superfluid phases are of first order. In a real experiment, where fermion numbers are approximately conserved for each component, such first-order transitions would appear as segregation of different SF phases, and domain formation.[16] Experimentally, these domains would likely appear as a shell structure, sketched in Fig. 15. Based upon our phase diagram, for $N_3 > N_2 \gtrsim N_1$, e.g., a possible configuration is that in the center of the trap a (23) superfluid forms, however, approaching the external region of the trap T_c decreases, and the (12) superfluid state becomes more stable.[72] Similar shell-like structures have been proposed, e.g., in the case of unequal masses of the three fermionic components.[73] We remark, however that phase separation in a trap can be more complicated when the total numbers of atoms N_1, N_2, and N_3 is such that they restrict the local chemical potentials in the trap to follow the SF-SF phase boundaries in our phase diagram, e.g., in the case of $N_3 \gtrsim N_1 = N_2$. In this case, we can not give a simple argument on the possible phase configurations. We also remark that in case of strong interactions, strong spontaneous magnetization most likely leads to phase separation even in the SU(3) symmetric case $N_1 = N_2 = N_3$, as suggested in Refs. 16,24 and also found in Ref. 25 in case of a lattice with strong three-particle losses, and in Ref. 40 in the continuum.

As a rule of thumb, SF order tends to form in the channel of the smallest chemical potential difference. This simple rule determines the overall structure of the phase diagram (see Fig. 7). However, unlike the two-component case, for three-component mixtures a nontrivial coupling between magnetic and SF order is also allowed.[16,24] This interesting coupling, the strength of which is regulated by particle-hole symmetry breaking $\gamma \sim \varrho'(E_F)/\varrho(E_F) \sim 1/E_F$, leads to a peculiar triangular structure in the central region of the phase diagram $\mu_i \approx \mu$, in agreement with the predictions of Ref. 24 (although with opposite orientation, see Fig. 7). However, the relative size of this central region is apparently proportional to $\sim\sqrt{\gamma T_c}$; therefore, for weak and intermediate couplings, the triangular structure appears only in the close vicinity of the SU(3) symmetrical point $\mu_i \equiv \mu$. For very strong attractive interactions $T_c \approx E_F \sim W$, on the other hand, the central (triangular) region must get more extended, and may become observable.

We also constructed the Ginzburg-Landau functionals describing the three-component mixture, and determined the temperature and asymmetry (γ) dependence of the various coefficients. We have shown that, to capture the termination of the central triangular region, one needs to go beyond the expansion of Ref. 24, and higher-order terms need be incorporated in the functionals.

As discussed in Sec. V, fluctuations modify somewhat the mean-field picture. The temperature-driven phase transition for generic (unequal) chemical potential values is typically described by the XY model and its critical exponents. However, for certain special chemical potentials, the competition between various superfluid orders may lead to interesting critical behavior. For $\mu_i \equiv \mu$ and an SU(3) symmetrical interaction, e.g., the normal-SF transition belongs to the O(6) universality class, and is characterized by the corresponding exponents. Along the critical lines separating the three phases (12), (23), and (31), on the other hand, an interesting O(2,2) critical behavior may emerge (see our discussion in Sec. V). The shape of the phase diagram in the vicinity of these special lines is then determined by the corresponding universal crossover exponents. We emphasize that, while it is very difficult to observe it in the weak-coupling regime, a nontrivial critical behavior could be observable in the strong-coupling regime, often reached in cold-atom experiments.

Finally, we studied the fragility of the SU(3) physics, i.e., the sensitivity of these results and the phase diagram to the symmetry of interaction. We have shown that already a small difference in the scattering lengths can substantially distort the SU(3) phase diagram, and the SF phase of the channel with the strongest interaction may suppress and mask the SU(3) symmetrical [O(6)] critical regime. These results agree with those obtained in Ref. 70. Here, however, in contrast to Ref. 70, we focused on the consequences of SU(3) symmetry (rather than on the consequences of its violation) and the effects of the coupling between ferromagnetic and superfluid order parameters, neglected in Ref. 70. In addition, we also discussed the role of fluctuations and the structure of the emerging critical states and multicritical lines. Our results as well as those of Ref. 70 indicate that in experimental realizations, to observe the SU(3) physics, one should use systems with almost perfectly symmetrical interactions, similar to Yb,[74] or one should use some tricks to make all scattering lengths equal as much as possible.[28] Moreover, one should possibly stay in the strong-coupling regime $T_c \sim W$, where the impact of a small asymmetry in the interaction is not exponentially large.

ACKNOWLEDGMENTS

We would like to thank E. Demler, G. Refael, and W. Hofstetter for enlightening discussions. This research has been supported by the Hungarian research funds OTKA and NKTH under Grants No. K73361 and No. CNK80991. G.Z. acknowledges support from the Humboldt Foundation and the DFG.

APPENDIX A: EXACT WARD IDENTITIES

In this Appendix, by making use of the global SU(3) invariance of the functional measure, we derive exact Ward identities that give constraints on the possible values of the order parameters and densities [Eqs. (6)–(9)]. Consider the partition function $\mathcal{Z}$, defined in Eq. (12). For the current calculation, we rewrite the action in equations (13) and (14) in the form

$$S_0(\hat{\mu}) = \sum_{\alpha\beta} \int dx\, \overline{\psi}_\alpha [(\partial_\tau + \mathcal{H}_0)\delta_{\alpha\beta} - \hat{\mu}_{\alpha\beta}]\psi_\beta, \tag{A1}$$

$$S_{\text{int}}(\Gamma) = -\sum_{\alpha\beta\gamma\delta} \Gamma_{\alpha\beta\gamma\delta} \int dx\, \overline{\psi}_\alpha \overline{\psi}_\beta \psi_\gamma \psi_\delta \tag{A2}$$

by introducing $\hat{\mu}_{\alpha\beta} = \mu_\alpha\, \delta_{\alpha\beta}$ and $\Gamma_{\alpha\beta\gamma\delta} = \frac{1}{2}\lambda_{\alpha\beta}(\delta_{\alpha\delta}\delta_{\beta\gamma} - \delta_{\alpha\gamma}\delta_{\beta\delta})$. An SU(3) transformation of the fields $\psi_\alpha(x) \to \sum_\beta U_{\alpha\beta}\psi_\beta(x)$ translates to the transformation of $\hat{\mu}$ and Γ in the functional integral. Expressing $\mathbf{U} = \exp(i\sum_{a=1}^{8}\eta^a \mathbf{T}^a)$ with the Gell-Mann matrices $\mathbf{T}^a$, we find

$$\left.\frac{\partial}{\partial\eta^a}\hat{\mu}_{\alpha\beta}(\eta)\right|_{\eta^a=0} = i\sum_\gamma \left(\hat{\mu}_{\alpha\gamma}T^a_{\gamma\beta} - T^a_{\alpha\gamma}\hat{\mu}_{\gamma\beta}\right), \tag{A3}$$

$$\left.\frac{\partial}{\partial\eta^a}\Gamma_{\alpha\beta\gamma\delta}(\eta)\right|_{\eta^a=0} = 2i(\lambda_{\alpha\beta} - \lambda_{\gamma\delta})\delta_{\alpha\delta}\, T^a_{\beta\gamma}. \tag{A4}$$

The invariance of the functional integral with respect to global SU(3) transformations $\frac{\partial\mathcal{Z}}{\partial\eta^a}|_{\eta_a=0} = 0$ leads to the Ward identity

$$(\mu_\alpha - \mu_\beta)\frac{\partial \ln\mathcal{Z}}{\partial\hat{\mu}_{\alpha\beta}} = 2\sum_\gamma(\lambda_{\beta\gamma} - \lambda_{\alpha\gamma})\frac{\partial \ln\mathcal{Z}}{\partial\Gamma_{\gamma\alpha\beta\gamma}} \tag{A5}$$

for any α and β, from which Eq. (32) follows.

APPENDIX B: WARD IDENTITIES IN THE GAUSSIAN APPROXIMATION

Here, we derive approximate Ward identities, similar to those in Appendix A, that hold in the Gaussian approximation. As explained in Appendix C, we can assume that the inverse propagator in the definition of the partition function $\mathcal{Z}_\mathcal{D}$ [Eq. (18)] is local:

$$\mathcal{Z}_\mathcal{D} = \int \mathfrak{D}\overline{\boldsymbol{\psi}}\,\mathfrak{D}\boldsymbol{\psi}\; e^{\frac{1}{2}\int d1\,\overline{\phi}(1)\mathbf{D}^{-1}(1)\phi(1)}, \tag{B1}$$

where $\mathbf{D}^{-1}$ is defined in Eq. (23).

An SU(3) transformation of the fields $\psi_\alpha(x) \to \sum_\beta U_{\alpha\beta}\psi_\beta(x)$ translates to the transformation of order parameters

$$\boldsymbol{\Lambda} \mapsto \mathbf{U}\boldsymbol{\Lambda}\mathbf{U}^+, \tag{B2}$$

$$\boldsymbol{\Delta} \mapsto \mathbf{U}\boldsymbol{\Delta}\mathbf{U}^\mathrm{T} \tag{B3}$$

[see Eqs. (29) and (30)]. Using the invariance of the partition function with respect to these global SU(3) transformations, we get the following constraints on the densities:

$$\mathrm{Tr}\left[\begin{pmatrix} \boldsymbol{\Gamma}^a_{\boldsymbol{\Lambda}} & \boldsymbol{\Gamma}^a_{\boldsymbol{\Delta}} \\ -\boldsymbol{\Gamma}^{a+}_{\boldsymbol{\Delta}} & \boldsymbol{\Gamma}^{a*}_{\boldsymbol{\Lambda}} \end{pmatrix}\begin{pmatrix} -\mathbf{n}^* & \mathbf{d} \\ \mathbf{d}^+ & \mathbf{n} \end{pmatrix}\right] = 0, \tag{B4}$$

with $\boldsymbol{\Gamma}^a_{\boldsymbol{\Lambda}} = [\boldsymbol{\Lambda},\mathbf{T}^a]$ and $\boldsymbol{\Gamma}^a_{\boldsymbol{\Delta}} = 2(\mathbf{T}^a\boldsymbol{\Delta} + \boldsymbol{\Delta}\mathbf{T}^{a*})$.[75] Here, the matrices $\mathbf{T}^a$, $a = 1,\ldots,8$, are the Gell-Mann matrices.

In the case of SU(3) symmetric interactions, at the solutions of the EOM equations [Eqs. (6), (7), and (10)], this equation simplifies to the same form as the exact Ward identity [Eq. (32)]:

$$(\mu_\alpha - \mu_\beta)n_{\alpha\beta} = 0\,. \tag{B5}$$

Therefore, when neither two of the chemical potentials are equal, the matrix of densities $\mathbf{n}$ and that of renormalized chemical potentials $\boldsymbol{\Lambda}$ are both diagonal [see Eq. (7)].

APPENDIX C: SADDLE-POINT EQUATION IN THE GAUSSIAN APPROXIMATION

In this Appendix, starting from the saddle-point equation (21), we derive the saddle-point form of the propagator $\mathcal{D}$ in the Gaussian approximation [Eqs. (22) and (23)]. We will use the notations of Sec. II B.

First, we fix the arbitrariness in the form of $\mathcal{D}^{-1}$ in the definition of $S_\mathcal{D}$ [Eq. (17)]. We split $\mathcal{D}^{-1}$ into 3×3 matrices

$$\mathcal{D}^{-1}(1,2) = \begin{pmatrix} \boldsymbol{\Gamma}_A(x_1,x_2) & \boldsymbol{\Gamma}_B(x_1,x_2) \\ \boldsymbol{\Gamma}_C(x_1,x_2) & \boldsymbol{\Gamma}_D(x_1,x_2) \end{pmatrix}. \tag{C1}$$

It is easy to see that, because of the anticommutation of the fields $\overline{\psi}_\alpha$ and ψ_α, modifications of $\mathcal{D}^{-1}$ that leave $\mathbf{\Gamma}_A(x_1,x_2) - \mathbf{\Gamma}_D^T(x_2,x_1)$, $\mathbf{\Gamma}_B(x_1,x_2) - \mathbf{\Gamma}_B^T(x_2,x_1)$, and $\mathbf{\Gamma}_C(x_1,x_2) - \mathbf{\Gamma}_C^T(x_2,x_1)$ invariant, will not change $S_{\mathcal{D}}$. Therefore, we may assume that $\mathcal{D}^{-1}$ has the symplectic symmetry

$$\begin{pmatrix} \mathbf{0} & \mathbf{1} \\ \mathbf{1} & \mathbf{0} \end{pmatrix} \mathcal{D}^{-1}(x_1,x_2) \begin{pmatrix} \mathbf{0} & \mathbf{1} \\ \mathbf{1} & \mathbf{0} \end{pmatrix} = -(\mathcal{D}^{-1})^{\mathrm{T}}(x_2,x_1). \quad \text{(C2)}$$

The saddle-point equation (21) gives very strong constraints on the form of $\mathcal{D}$. In particular, it is equivalent to the EOM self-consistency equation of Sec. II A. To see this, we use the definition (16) to rewrite Eq. (21) in the form

$$\frac{1}{\mathcal{Z}_{\mathcal{D}}} \frac{\delta \mathcal{Z}_{\mathcal{D}}}{\delta \mathcal{D}(1,2)} = \frac{\delta \langle S - S_{\mathcal{D}} \rangle_{\mathcal{D}}}{\delta \mathcal{D}(1,2)}. \quad \text{(C3)}$$

The calculation of the left-hand side of this equation is straightforward. Using only the definition of $\mathcal{Z}_{\mathcal{D}}$ [see Eq. (18)] and Eq. (20), we get

$$\frac{1}{\mathcal{Z}_{\mathcal{D}}} \frac{\delta \mathcal{Z}_{\mathcal{D}}}{\delta \mathcal{D}(1,2)} = -\frac{1}{2} \mathcal{D}^{-1}(2,1). \quad \text{(C4)}$$

To evaluate the right-hand side of Eq. (C3), omitting a constant term, we can write

$$\langle S - S_{\mathcal{D}} \rangle_{\mathcal{D}} = -\frac{1}{2} \int d1\, d2\, \mathcal{D}_0^{-1}(1,2) \mathcal{D}(2,1) + \langle S_{\mathrm{int}} \rangle_{\mathcal{D}}. \quad \text{(C5)}$$

Then, it is easy to see that the saddle-point equation is equivalent to

$$\mathcal{D}^{-1}(1,2) = \mathcal{D}_0^{-1}(1,2) - 2\, \frac{\delta \langle S_{\mathrm{int}} \rangle_{\mathcal{D}}}{\delta \mathcal{D}(2,1)}. \quad \text{(C6)}$$

Expanding $\langle S_{\mathrm{int}} \rangle_{\mathcal{D}}$ using Wick's theorem gives a product of equal-time propagators, whose variation according to the propagator matrix $\mathcal{D}$ can be straightforwardly calculated. We get the desired formulas (22) and (23), with the order parameters $\mathbf{\Lambda}$ and $\mathbf{\Delta}$ satisfying the EOM self-consistency equations (6), (7), and (10). This means that the EOM method is *consistent* with the Gaussian variational approach.

APPENDIX D: CALCULATION OF THE GAUSSIAN APPROXIMATION TO THE FREE ENERGY

In the following, we calculate the Gaussian approximation of the free energy, Eq. (25). We first introduce the Fourier components $\psi_\alpha(\mathbf{r}) = \frac{1}{\sqrt{\Omega}} \sum_{\mathbf{k}} e^{i\mathbf{kr}} a_{\alpha\mathbf{k}}$, obeying the anticommutation relations $\{a^\dagger_{\mathbf{k}\alpha}, a_{\mathbf{k}'\beta}\} = \delta_{\alpha\beta}\, \delta_{\mathbf{kk}'}$, where Ω denotes the volume. With these, the Hamiltonian (24) takes on the form

$$H_{\mathcal{D}} = \frac{1}{2} \sum_{\mathbf{k}} \left\{ (\mathbf{a}^\dagger_{\mathbf{k}}, \mathbf{a}_{-\mathbf{k}}) \mathbf{B}(\xi_{\mathbf{k}}) \begin{pmatrix} \mathbf{a}_{\mathbf{k}} \\ \mathbf{a}^\dagger_{-\mathbf{k}} \end{pmatrix} + \mathrm{Tr}(\xi_{\mathbf{k}} - \mathbf{\Lambda}) \right\}, \quad \text{(D1)}$$

with $\mathbf{B}(\xi)$ defined in Eq. (5), and the last term originating from normal ordering.

From the above form, the calculation of $\mathcal{Z}_{\mathcal{D}} = \mathrm{Tr} e^{-\beta H_{\mathcal{D}}}$ is straightforward, although some care is needed to avoid double counting in momentum space. Note that because of the symplectic symmetry [Eq. (11)] and Hermiticity of the matrix $\mathbf{B}(\xi)$, its eigenvalues are real and come in pairs. To each eigenvalue $\eta(\xi)$ there is another eigenvalue $-\eta(\xi)$. Using this property, $\ln \mathcal{Z}_{\mathcal{D}}$ simplifies to

$$\ln \mathcal{Z}_{\mathcal{D}} = \frac{1}{2} \sum_{\mathbf{k}} \mathrm{Tr} \ln \left[2 \cosh \left(\frac{\beta}{2} \mathbf{B}(\xi_{\mathbf{k}}) \right) \right] - \frac{\beta}{2} \sum_{\mathbf{k}} \mathrm{Tr}(\xi_{\mathbf{k}} - \mathbf{\Lambda}). \quad \text{(D2)}$$

The calculation of $\langle H - H_{\mathcal{D}} \rangle_{\mathcal{D}}$ is also straightforward using Wick's theorem. One finds

$$\frac{1}{\Omega} \langle H - H_{\mathcal{D}} \rangle_{\mathcal{D}} = \sum_{\alpha\beta} \lambda_{\alpha\beta} (|n_{\alpha\beta}|^2 - n_{\alpha\alpha} n_{\beta\beta} - |d_{\alpha\beta}|^2) + \sum_{\alpha\beta} (\Lambda_{\alpha\beta} - \mu_\alpha \delta_{\alpha\beta}) n_{\alpha\beta} + \sum_{\alpha\beta} \Delta_{\alpha\beta} d^*_{\alpha\beta} + \Delta^*_{\alpha\beta} d_{\alpha\beta}. \quad \text{(D3)}$$

Thus, using Eqs. (D2) and (D3), we get the result (28) for the Gaussian approximation of the free-energy density. In order to evaluate Eq. (D3), the densities and anomalous densities $\mathbf{n}$ and $\mathbf{d}$ also have to be determined. These can be easily calculated from the variations of (D2) with respect to $\mathbf{\Lambda}$ and $\mathbf{\Delta}$, leading to the same equation [Eq. (10)] as the EOM self-consistency equations.

APPENDIX E: PARTICLE-HOLE TRANSFORMATION

Particle-hole symmetry introduces a $\mathbb{Z}_2$ symmetry of the mean-field phase diagram, when the band is half-filled, the DOS is particle-hole symmetric [$\rho(\xi) = \rho(-\xi)$], and the interaction has SU(3) symmetry ($\lambda_{\alpha\beta} = \lambda$ for $\alpha \neq \beta$). This symmetry together with the permutation symmetry of the fermion species make the phase diagram sixfold symmetric (see Fig. 1).

In this appendix, we calculate the effect of the particle-hole transformation

$$\Psi_\alpha(x) \longleftrightarrow \Psi^\dagger_\alpha(x) \quad \text{(E1)}$$

on the order parameters $\mathbf{\Lambda}$ and $\mathbf{\Delta}$. This transformation leaves the interaction invariant, whereas it modifies the bare chemical potentials and the single-particle energies as

$$\mathcal{H}_0 \to -\mathcal{H}_0, \quad \text{(E2)}$$

$$\mu_\alpha \to -\mu_\alpha - 4\lambda\, n_{\max}, \quad \text{(E3)}$$

where $n_{\max} = \int_{-W}^{W} d\xi\, \rho(\xi)$ is the density of the completely filled band. The bare chemical potentials remain unchanged on the mean-field level at

$$\mu_{\mathrm{half}} = -2\lambda\, n_{\max}, \quad \text{(E4)}$$

which is precisely the condition for the band being half-filled [see Eq. (7)].

In order to investigate the inversion symmetry of the phase diagram, consider two Hamiltonians with opposite differences in bare chemical potentials from half-filling:

$$H^{(1)} \equiv H(\mathcal{H}_0, \mu_{\mathrm{half}} + \delta\mu_\alpha, \lambda, \Psi^\dagger_\alpha, \Psi_\alpha), \quad \text{(E5)}$$

$$H^{(2)} \equiv H(\mathcal{H}_0, \mu_{\mathrm{half}} - \delta\mu_\alpha, \lambda, \Psi^\dagger_\alpha, \Psi_\alpha), \quad \text{(E6)}$$

as defined in Eq. (1). A particle-hole transformation of $H^{(2)}$ leads to the equation

$$H^{(2)} = H(-\mathcal{H}_0,\mu_{\text{half}} + \delta\mu_\alpha,\lambda,\widetilde{\Psi}_\alpha^\dagger,\widetilde{\Psi}_\alpha) \equiv H^{(3)}, \quad \text{(E7)}$$

where $\widetilde{\Psi}_\alpha = \Psi_\alpha^\dagger$. Accordingly, the densities in the original and the particle-hole-transformed system can be connected as

$$n_{\alpha\beta}^{(3)} \equiv \langle \widetilde{\Psi}_\alpha^\dagger(x)\widetilde{\Psi}_\beta(x)\rangle_{(3)} = -n_{\alpha\beta}^{(2)*} + n_{\max}, \quad \text{(E8)}$$

$$d_{\alpha\beta}^{(3)} \equiv \langle \widetilde{\Psi}_\alpha(x)\widetilde{\Psi}_\beta(x)\rangle_{(3)} = -d_{\alpha\beta}^{(2)*}. \quad \text{(E9)}$$

Then, it is also straightforward to show from the definitions (6) and (7) that the relation between the order parameters are

$$\mathbf{\Lambda}^{(2)} = -\mathbf{\Lambda}^{(3)*}, \quad \mathbf{\Delta}^{(2)} = -\mathbf{\Delta}^{(3)*}. \quad \text{(E10)}$$

Looking at their definitions, we see that the only difference between $H^{(2)}$ and $H^{(3)}$ is in the sign of $\mathcal{H}_0$. However, if the DOS is electron-hole symmetric,

$$\rho(\xi) = \rho(-\xi), \quad \text{(E11)}$$

then all of the EOM self-consistency equations (6), (7), and (10), and the mean-field free-energy equations (10) and (28) are identical in the two systems. Therefore, the set of the possible mean-field configurations have to be the same ($\mathbf{\Lambda}^{(1)} = \mathbf{\Lambda}^{(3)}$, $\mathbf{\Delta}^{(1)} = \mathbf{\Delta}^{(3)}$). Putting this, and Eq. (E10) together, we obtain the desired equations

$$\mathbf{\Lambda}(\mu_{\text{half}} + \delta\mu_\alpha) = -\mathbf{\Lambda}^*(\mu_{\text{half}} - \delta\mu_\alpha), \quad \text{(E12)}$$

$$\mathbf{\Delta}(\mu_{\text{half}} + \delta\mu_\alpha) = -\mathbf{\Delta}^*(\mu_{\text{half}} - \delta\mu_\alpha), \quad \text{(E13)}$$

connecting order parameters at opposite $\delta\mu_\alpha$ values, with the other parameters of the system unchanged.

We remark that in the special case when $\delta\mu_1 + \delta\mu_2 + \delta\mu_3 = 0$, the particle-hole symmetry connects the points of the same (μ_x,μ_y) plane, and the mean-field phase diagram has an inversion symmetry. Away from this plane, the inversion symmetry is only approximate due to logarithmic corrections to the values of the order parameters coming from the asymmetric cutoff.

---

[1] I. Bloch, J. Dalibard, and W. Zwerger, Rev. Mod. Phys. **80**, 885 (2008).

[2] M. P. A. Fisher, P. B. Weichman, G. Grinstein, and D. S. Fisher, Phys. Rev. B **40**, 546 (1989); D. Jaksch, C. Bruder, J. I. Cirac, C. W. Gardiner, and P. Zoller, Phys. Rev. Lett. **81**, 3108 (1998); M. Greiner, M. O. Mandel, T. Esslinger, T. Hänsch, and I. Bloch, Nature (London) **415**, 39 (2002).

[3] J. K. Chin, D. E. Miller, Y. Liu, C. Stan, W. Setiawan, C. Sanner, K. Xu, and W. Ketterle, Nature (London) **443**, 961 (2006).

[4] C. Chin, M. Bartenstein, A. Altmeyer, S. Riedl, S. Jochim, J. Hecker Denschlag, and R. Grimm, Science **305**, 1128 (2004); M. W. Zwierlein, C. A. Stan, C. H. Schunck, S. M. F. Raupach, A. J. Kerman, and W. Ketterle, Phys. Rev. Lett. **92**, 120403 (2004); C. A. Regal, M. Greiner, and D. S. Jin, *ibid.* **92**, 040403 (2004); J. Kinast, S. L. Hemmer, M. E. Gehm, A. Turlapov, and J. E. Thomas, *ibid.* **92**, 150402 (2004).

[5] M. W. Zwierlein, C. H. Schunck, A. Schirotzek, and W. Ketterle, Nature (London) **442**, 54 (2006).

[6] G. B. Partridge, W. Li, R. I. Kamar, Y. Liao, and R. G. Hulet, Science **311**, 503 (2006).

[7] M. W. Zwierlein, A. Schirotzek, C. H. Schunck, and W. Ketterle, Science **311**, 492 (2006).

[8] Y. Shin, C. H. Schunck, A. Schirotzek, and W. Ketterle, Nature (London) **451**, 689 (2008).

[9] M. W. Zwierlein, J. R. Abo-Shaeer, A. Schirotzek, C. H. Schunck, and W. Ketterle, Nature (London) **435**, 1047 (2005).

[10] M. R. Andrews, C. G. Townsend, H.-J. Miesner, D. S. Durfee, D. M. Kurn, and W. Ketterle, Science **275**, 637 (1997); K. W. Madison, F. Chevy, W. Wohlleben, and J. Dalibard, Phys. Rev. Lett. **84**, 806 (2000); O. M. Marago, S. A. Hopkins, J. Arlt, E. Hodby, G. Hechenblaikner, and C. J. Foot, *ibid.* **84**, 2056 (2000); C. Raman, M. Köhl, R. Onofrio, D. S. Durfee, C. E. Kuklewicz, Z. Hadzibabic, and W. Ketterle, *ibid.* **83**, 2502 (1999).

[11] K. E. Strecker, G. B. Partridge, A. G. Truscott, and R. G. Hulet, Nature (London) **417**, 150 (2002); L. Khaykovich, F. Schreck, G. Ferrari, T. Bourdel, J. Cubizolles, L. D. Carr, Y. Castin, and C. Salomon, Science **296**, 1290 (2002).

[12] L. S. Leslie, A. Hansen, K. C. Wright, B. M. Deutsch, and N. P. Bigelow, Phys. Rev. Lett. **103**, 250401 (2009); J. Ruostekoski and J. R. Anglin, *ibid.* **86**, 3934 (2001); C. M. Savage and J. Ruostekoski, *ibid.* **91**, 010403 (2003); V. Pietilä and M. Möttönen, *ibid.* **103**, 030401 (2009).

[13] E. Babaev, L. D. Faddeev, and A. J. Niemi, Phys. Rev. B **65**, 100512(R) (2002).

[14] Y.-J. Lin, R. L. Compton, K. Jiménez-García, J. V. Porto, and I. B. Spielman, Nature (London) **452**, 628 (2009); J. Dalibard, F. Gerbier, G. Juzeliunas, and P. Ohberg, Rev. Mod. Phys. **83**, 1523 (2011); N. R. Cooper, Phys. Rev. Lett. **106**, 175301 (2011).

[15] C. Honerkamp and W. Hofstetter, Phys. Rev. Lett. **92**, 170403 (2004).

[16] Á. Rapp, G. Zaránd, C. Honerkamp, and W. Hofstetter, Phys. Rev. Lett. **98**, 160405 (2007); Á. Rapp, W. Hofstetter, and G. Zaránd, Phys. Rev. B **77**, 144520 (2008).

[17] J. H. Huckans, J. R. Williams, E. L. Hazlett, R. W. Stites, and K. M. OHara, Phys. Rev. Lett. **102**, 165302 (2009); J. R. Williams, E. L. Hazlett, J. H. Huckans, R. W. Stites, Y. Zhang, and K. M. OHara, *ibid.* **103**, 130404 (2009).

[18] A. Kantian, M. Dalmonte, S. Diehl, W. Hofstetter, P. Zoller, and A. J. Daley, Phys. Rev. Lett. **103**, 240401 (2009).

[19] T. Kraemer, M. Mark, P. Waldburger, J. G. Danzl, C. Chin, B. Engeser, A. D. Lange, K. Pilch, A. Jaakkola, H.-C. Nägerl, and R. Grimm, Nature (London) **440**, 315 (2006).

[20] T. B. Ottenstein, T. Lompe, M. Kohnen, A. N. Wenz, and S. Jochim, Phys. Rev. Lett. **101**, 203202 (2008).

[21] A. V. Gorshkov, M. Hermele, V. Gurarie, C. Xu, P. S. Julienne, J. Ye, P. Zoller, E. Demler, M. D. Lukin, and A. M. Rey, Nat. Phys. **6**, 289 (2010).

[22] C. Wu, J. P. Hu, and S. C. Zhang, Phys. Rev. Lett. **91**, 186402 (2003).

[23] D. S. Sarma, J. Phys. Chem. Solids **24**, 1029 (1963).

[24] R. W. Cherng, G. Refael, and E. Demler, Phys. Rev. Lett. **99**, 130406 (2007).

[25] I. Titvinidze, A. Privitera, S.-Y. Chang, S. Diehl, M. A. Baranov, A. Daley, and W. Hofstetter, New J. Phys. **13**, 035013 (2011).

[26] Note that our convention for the interaction strength differs from the usual convention by a factor of 1/2. This difference also affects the definitions of the order parameters later [see Eqs. (6) and (7)].

[27] M. Bartenstein, A. Altmeyer, S. Riedl, R. Geursen, S. Jochim, C. Chin, J. H. Denschlag, R. Grimm, A. Simoni, E. Tiesinga, C. J. Williams, and P. S. Julienne, Phys. Rev. Lett. **94**, 103201 (2005).

[28] K. M. O'Hara, New J. Phys. **13**, 065011 (2011).

[29] Notice that the chemical potentials in Eq. (1) are chosen to be zero in the middle of the single-particle energy band $\xi = 0$.

[30] C. Honerkamp and W. Hofstetter, Phys. Rev. B **70**, 094521 (2004).

[31] Part of the interaction is decomposed in the superfluid channel, while the other part in the ferromagnetic channel, and thus part of the interaction energy is apparently dropped.

[32] P. Fulde and R. A. Ferrell, Phys. Rev. **135**, A550 (1964).

[33] A. I. Larkin and Yu. N. Ovchinnikov, Zh. Eksp. Teor. Fiz. **47**, 1136 (1964) [Sov. Phys. JETP **20**, 762 (1965)].

[34] W. V. Liu and F. Wilczek, Phys. Rev. Lett. **90**, 047002 (2003); Michael McNeil Forbes, E. Gubankova, W. V. Liu, and F. Wilczek, *ibid.* **94**, 017001 (2005).

[35] This is a standard BCS approximation for T_c in case of constant DOS [see M. Tinkham, *Introduction to Superconductivity* (McGraw-Hill, New York, 1996)]. A straightforward generalization of this BCS calculation to the case of linear DOS leads to the result $T_c \approx 1.13\sqrt{W^2 - \xi_F^2}e^{-1/(2\lambda\rho_F)}e^{-(\rho_F-\rho_0)/\rho_F}$, which is an accurate estimate of T_c in the weak-coupling regime, for arbitrary values of γ.

[36] Throughout the text, we shall refer to the critical temperature at the SU(3) symmetric point as T_c.

[37] In the $\gamma = 0$ case, the mean-field equations are particle-hole symmetric only at a special chemical potential value, corresponding to half-filling. Nevertheless, for $\gamma = 0$ particle-hole symmetry holds in the weak-coupling regime for a wide range of equal chemical potentials ($\mu_\alpha \equiv \bar{\mu}$) as an *approximate symmetry*, as we explain in Sec. II C. On the other hand, this (approximate) symmetry is broken by any $\gamma \neq 0$.

[38] The average of the chemical potentials $\bar{\mu} \equiv (\mu_1 + \mu_2 + \mu_3)/3$ does not have a considerable effect on the phase diagrams due to (approximate) particle-hole symmetry in the $\gamma = 0$ case (see Sec. II C).

[39] This pairing process is similar to that of two-component SF (see Ref. 23) to enable Cooper-pair formation, the Fermi surfaces of the two species must be shifted. Pairing results in a condensation energy gain, whereas the shift of the Fermi surfaces results in a kinetic energy loss. The latter is minimal if components with the smallest chemical potential difference pair up.

[40] T. Ozawa and G. Baym, Phys. Rev. A **82**, 063615 (2010).

[41] Of course, particle-hole symmetry can be broken in many other ways, too (by introducing an asymmetrical cutoff $W_\pm$, e.g.), but the nonvanishing slope of the DOS seems to have the largest impact.

[42] We remark that our definition of the SF order parameter $\Delta_{\alpha\beta}$ differs from the usual convention by a factor of 1/2. This comes from the factor 1/2 difference in our convention for the interaction parameter $\lambda_{\alpha\beta}$ in Eq. (2).

[43] R. P. Feynman, *Statistical Mechanics: A Set of Lectures*, 2nd ed. (Perseus Books Group, New York, 1998).

[44] We verified that, indeed, this normal ordering provides the correct densities at the free-energy minima.

[45] A. M. Clogston, Phys. Rev. Lett. **9**, 266 (1962).

[46] In case of a linear DOS, $T_c^{(*)}$ is slightly greater than T_c for positive μ_y's, while it is slightly smaller than T_c for $\mu_y < 0$.

[47] Our result for the case $T_c/W = 0.1$ is only an estimate since our mean-field equations can not be considered accurate in the regime of intermediate interactions (see Ref. 40).

[48] Since the simultaneous shift of all the chemical potential components shall have no impact apart from changing the value of the Ginzburg-Landau coefficients, we restrict ourselves to $\mathrm{Tr}\delta\tilde{\boldsymbol{\mu}} = 0$.

[49] Notice that the term $[\mathrm{Tr}(\widetilde{\boldsymbol{\Delta}}\widetilde{\boldsymbol{\Delta}}^+)]^2$ is proportional to $\mathrm{Tr}[(\widetilde{\boldsymbol{\Delta}}\widetilde{\boldsymbol{\Delta}}^+)^2]$, and does not appear in the expansion.

[50] Z. Hadzibabic, P. Krüger, M. Cheneau, B. Battelier, and J. Dalibard, Nature (London) **441**, 1118 (2006).

[51] H. Kleinert, J. Neu, V. Schulte-Frohlinde, K. G. Chetyrkin, and S. A. Larin, Phys. Lett. B **272**, 39 (1991).

[52] S. A. Antonenko and A. I. Sokolov, Phys. Rev. E **51**, 1894 (1995).

[53] P. Butera and M. Comi, Phys. Rev. B **56**, 8212 (1997).

[54] D. Loison, Phys. A (Amsterdam) **271**, 157 (1999).

[55] J. Cardy, *Scaling and Renormalization in Statistical Physics*, Cambridge Lecture Notes in Physics (Cambridge University Press, Cambridge, 1996).

[56] M. Campostrini, M. Hasenbusch, A. Pelissetto, P. Rossi, and E. Vicari, Phys. Rev. B **63**, 214503 (2001); R. Guida and J. Zinn-Justin, J. Phys. A: Math. Gen. **31**, 8103 (1998).

[57] J. M. Kosterlitz and D. J. Thouless, J. Phys. C: Solid State Phys. **6**, 1181 (1973).

[58] In the absence of particle-hole symmetry, one may need to rescale the fields Δ_{23} and Δ_{13} to have the same coefficient in the kinetic part.

[59] J. M. Kosterlitz, D. R. Nelson, and M. E. Fisher, Phys. Rev. B **13**, 412 (1976).

[60] E. Brezin, J. C. Le Guillou, and J. Zinn-Justin, Phys. Rev. B **10**, 892 (1974); D. Mukamel and S. Krinsky, *ibid.* **13**, 5065 (1976); **13**, 5078 (1976); E. Domany, D. Mukamel, and E. Fisher, *ibid.* **15**, 5432 (1977); J. C. Toledano, L. Michel, P. Toledano, and E. Brezin, *ibid.* **31**, 7171 (1985); M. Dudka, Y. Holovatch, and T. Yavors'kii, J. Phys. A: Math. Gen. **37**, 10727 (2004).

[61] A. Aharony, in *Phase Transitions and Critical Phenomna, Volume 6*, edited by C. Domb and M. S. Green (Academic, New York, 1977).

[62] D. Mukamel, Phys. Rev. Lett. **34**, 481 (1975).

[63] P. Calabrese, A. Pelissetto, and E. Vicari, Phys. Rev. B **67**, 054505 (2003).

[64] E. Vicari and J. Zinn-Justin, New J. Phys. **8**, 321 (2006).

[65] A. Aharony and S. Fishman, Phys. Rev. Lett. **37**, 1587 (1976); R. A. Cowley and A. D. Bruce, J. Phys. C: Solid State Phys. **11**, 3577 (1978); A. Aharony, Phys. Rev. Lett. **88**, 059703 (2002).

[66] M. Kanász-Nagy (unpublished). The estimate is based on the linear approximation of the DOS $\rho_{\mathrm{Li}}(\epsilon)$ around the Fermi energy ϵ_F of the experimental system; we choose the DOS to be $\rho(\xi) \equiv \rho_{\mathrm{Li}}(\epsilon_F) + \rho'_{\mathrm{Li}}(\epsilon_F)(\xi - \xi_F)$, and the cutoff $\pm W$ is chosen such that we get the same atom density for $\xi_F = 0$ as in the experimental system. We determine the interaction parameter $\lambda_{\alpha\beta}$ from that of the ^{6}Li system, $\lambda_{\alpha\beta}^{\mathrm{Li}}$, such that (summing up the ladder diagrams in the Cooper channel) the interaction vertex be equal in the two systems, leading to the equation $\frac{1}{2\lambda_{\alpha\beta}} - \frac{1}{2}\int d\xi\rho(\xi)\tanh(\frac{\xi-\xi_F}{2T})/(\xi - \xi_F) \approx \frac{1}{2\lambda_{\alpha\beta}^{\mathrm{Li}}} - \frac{1}{2}\int d\epsilon\rho_{\mathrm{Li}}(\epsilon)\tanh(\frac{\epsilon-\epsilon_F}{2T})/(\epsilon - \epsilon_F)$, for small values of T above T_c ($\epsilon_F \gg T > T_c$). Here, $\lambda_{\alpha\beta}^{\mathrm{Li}}$ is determined from the the scattering lengths $a_{\alpha\beta}$ using a similar calculation, but for $\epsilon_F \to 0$, leading to the standard result $\frac{m}{4\pi\hbar^2 a_{\alpha\beta}} = \frac{1}{2\lambda_{\alpha\beta}^{\mathrm{Li}}} - \frac{1}{2}\int d\epsilon\rho_{\mathrm{Li}}(\epsilon)/\epsilon$ (see Refs. 40 and 67).

[67] A. J. Leggett, in *Modern Trends in the Theory of Condensed Matter*, edited by A. Pekalski and J. Przystawa (Springer, Berlin, 1980).

[68] We remark that aside from the SF and magnetic ordering considered here, other phases that are beyond our mean-field approach (e.g., charge density waves) may appear in a lattice system.

[69] T. Paananen, J.-P. Martikainen, and P. Törmä, Phys. Rev. A **73**, 053606 (2006).

[70] G. Catelani and E. A. Yuzbashyan, Phys. Rev. A **78**, 033615 (2008).

[71] In an experimental situation, an appropriate definition of the weak-coupling limit is $T_c \ll E_F$, with E_F the Fermi energy. This is consistent with our previous definition $T_c \ll W$ since in our calculations we chose $E_F \approx W$, with E_F measured from the bottom of the band.

[72] In a parabolic trap configuration, described within the LDA approximation, the chemical potentials shift simultaneously and equally along the radial direction in the trap. In case of $\gamma > 0$, such a simultaneous shift leads to the decrease of T_c [with a simultaneous increase in $\gamma \leftrightarrow \rho(\epsilon_F)/\rho'(\epsilon_F)$] (Ref. 66) and therefore to the shrinkage of the phase diagram Fig. 3 in terms of μ_x/T_c, μ_y/T_c, and T/T_c. Therefore, ignoring the change in γ, the phase configuration of a parabolic trap at temperature T and with parameters μ_{x0}, μ_{y0}, and T_{c0} at the center of the trap, can be described by a straight line in our phase diagram, pointing outwards from the $(\mu_{x0}/T_{c0}, \mu_{y0}/T_{c0}, T/T_{c0})$ point. If the line intersects an SF-SF phase boundary, we expect a shell structure of superfluid phases, and a normal phase surrounding them. Such a situation is possible, e.g., in the case $N_3 > N_2 \gtrsim N_1$, with the line starting close to the horizontal (23)-(13) phase boundary on the bottom figure of Fig. 3. Of course, real experiments are much more complicated due to, e.g., a nonlinear DOS, elongated trap configurations, the effects of strong interactions, or non-LDA behavior.

[73] T. Paananen, P. Torma, and J.P. Martikainen, Phys. Rev. A **75**, 023622 (2007).

[74] M. Kitagawa, K. Enomoto, K. Kasa, Y. Takahashi, R. Ciurylo, P. Naidon, and P. S. Julienne, Phys. Rev. A **77**, 012719 (2008).

[75] We note that Eq. (B4) holds only at the solutions of the EOM self-consistency equations.